Center for Research in Electro-Optics and Lasers

AD-A242 751 **CREOL**

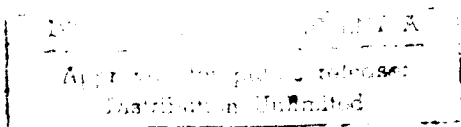## FINAL REPORT

TO

OFFICE OF NAVAL RESEARCH

ONR Contract No. N00014-89-K-0125

July 1991

UNIVERSITY OF CENTRAL FLORIDA
12424 Research Parkway
Orlando, FL 32826

91-14134

91 10 28 029

FINAL REPORT

TO

OFFICE OF NAVAL RESEARCH

ONR Contract No. N00014-89-K-0125

July 1991

prepared by

Center for Research in Electro Optics and Lasers (CREOL)

Task I. One Micron Coherent Laser Radar
Philip Gatt, Ph.D.

Task II. Atmospheric Seeing Measurements
Arthur R. Weeks, Ph.D.

Task III. Atmospheric Induced Enhanced Backscatter Characterization
Ron Phillips, Ph.D.

Task IV. IR Focal Plane Array Testing
Glenn Boreman, Ph.D.

Statement A per telecon Mathew White
ONR/Code 126
Arlington, Va   22217-5000

NWW 11/21/91

TABLE OF CONTENTS

ii

1. INTRODUCTION AND SUMMARY

This is the final report on ONR contract no. N00014-89-K-0125 for the Center for Research in Electro-Optics and Lasers (CREOL) at the University of Central Florida (UCF) to provide basic scientific support to the Innovative Science and Technology Experimental Facility (ISTEF) at Kennedy Space Center (KSC). The purpose of this program was to provide support to ISTEF in developing and testing innovative laser radar techniques and instrumentation for the discrimination and tracking of boosters, PBV's, and mid-course targets. This reporting period covers the full period of the contract, from April 1, 1989 to December 31, 1990. Under this contract, specific CREOL support to ISTEF included the following four tasks:

    Task I.   One Micron Coherent Laser Radar,

    Task II. Atmospheric Seeing Measurements,

    Task III. Atmospheric Induced Enhanced Backscatter Characterization,

    Task IV. IR Focal Plane Array Testing.

1.1 Task I. One Micron Coherent Laser Radar

The initial goal of the one micron task was to mechanically harden an existing coherent laser radar system that was to be supplied as government furnished equipment (GFE). Accomplishments toward this goal were inhibited by the lack of the delivery of the government laser which resulted in the adoption of an alternate program to design and construct an alternate laser radar system. Further delays were incurred as a result of the late delivery of a GFE transmitter which was to be utilized in this alternate ladar. As a result of these difficulties accomplishments toward the development of a one micron coherent laser radar were hindered. CREOL's accomplishments included the procurement, fabrication, test and calibration of the ladar subsystems to include: 1) a local oscillator, 2) an off axis Newtonian telescope, 3) a 2 Ghz InGaAs p-i-n detector, 4) a low noise high gain high bandwidth preamplifier, and 5) assorted high power AR coated 1.06 μm optics.

2

1.2 Task II. Atmospheric Seeing Measurements

The goal of this task was to develop a measurement capability at ISTEF to quantify the atmospheric seeing. "Seeing" through the atmosphere is degraded by turbulent fluctuations in the atmospheric refractive index. CREOL successfully demonstrated the use of an experimental setup consisting of a telescope and a video camera to measure the atmospheric seeing. The seeing is quantified by the Fried parameter, r_o. Using this CREOL-developed instrumentation, it was shown that at 5 μm and for "good" seeing conditions at ISTEF and a near vertical path, r_o was on the order of 14 cm.

1.3 Task III. Atmospheric Induced Enhanced Backscatter Characterization

The goal of this task was to characterize enhanced backscatter (EBS), which occurs to a laser beam when it passes through the same turbulent atmosphere twice. The double passage occurs in mono-static radar systems. The phenomenon was simulated on a computer, and numerical experiments conducted. Laboratory experiments were conducted on a laser beam passing twice through a random phase screen. The EBS signal was found with simple averaging of a TV image. Joint work was conducted with the British MoD Royal Signals and Radar Establishment on an outdoor 1000 meter range experiment. The averaging of TV images clearly shows diffraction limited information as to the target location.

1.4 Task IV. IR Focal Plane Array Testing

CREOL's Focal Plane Array testing program consists of the measurement of various specific detectors, the development of various instrumentation devices for the measurement of detector modulation transfer functions (MTFs), the development of an IR scene projector system as well as the development of data processing and computing facilities.

A new technique, utilizing a speckle generator, for the measurement of the detector modulation transfer function (MTF) has been developed. For the first time MTF measurements of hexagonal arrays, utilized in super-centroiding applications, have been reported.

2. ONE MICRON LASER RADAR

Philip Gatt, Ph.D.
Laser Radar Laboratory/CREOL

2.1 Background

The goal of this task was to provide ISTEF with a one micron ladar capability and for plume backscatter measurements and for evaluation and development of innovative ladar systems and components. A coherent one micron ladar will provide IST with a target discrimination and tracking capability, providing an increased (10 times) resolution over that of the more mature ten micron coherent ladar technology. Significant scientific innovations that relate specifically to shorter wavelength ladars should be investigated. These innovations include the use of tracking local oscillator, required for the larger anticipated doppler shifts, a fiber mixer/coupler to improve system ruggedness, and an array receiver to enhance the signal-to-noise ratio (SNR) in the presence of atmospheric turbulence

The initial task of CREOL's one micron ladar program was to mechanically harden an existing laboratory grade GFE 1.0J, Nd:YAG coherent laser radar system for field operation in an on-the-mount configuration. This laser radar system was to be supplied by another government contractor. Due to difficulties associated with the delivery of this government asset, CREOL was directed to design and construct an alternate prototype laser radar system to be deployed at ISTEF. This coherent ladar system would incorporate a 10cm monostatic off-axis transceiver and a government furnished 1.2J 20Hz 1.06μm laser purchased through Patrick Air Force Base (PAFB). Purchasing delays at PAFB resulted in a late delivery (January 1991) of this laser. During the PAFB laser procurement cycle, CREOL purchased, fabricated, and tested the major subsystems for the 1.06μm coherent ladar system.

Due to changing scientific goals CREOL was redirected in January of 1991 to design and fabricate a direct-detected one micron laser radar rather than a coherent laser radar, for the purpose of conducting plume backscatter measurements and an autodyne experiment, after which

3

4

the CREOL coherent laser radar program was to be resumed. The plume backscatter and the autodyne experiments will utilize a Contraves bistatic 10cm Coude' feed transmitter and 50cm pseudo-Cassegrain receiver telescope and mount system. This telescope is scheduled for ISTEF delivery from San Diego in the fall of 1991.

The autodyne experiment is a "proof of concept," active (532nm) target tracking experiment. This concept tracks the target at the plume/hardbody interface by maintaining a track on a "self-beat" note generated by a velocity difference between the hardbody of the target and its plume. The plume backscatter experiment will employ a direct detected laser radar to generate plume cross section/reflectance data at both 1064 and 532 nm. These data will be collected for an ensemble of "targets of opportunity" available to the ISTEF range.

2.2 Coherent Laser Radar Development

During the PAFB procurement cycle of the laser, major subsystems for the coherent receiver (Figure 2-1) were purchased, fabricated, and tested. These subsystems include: 1) an off-axis eccentric pupil 10X 10cm beam expander to be employed as the monostatic transceiver, 2) a single-mode diode-pumped 5mW CW Nd:YAG monolithic ring laser with fast PZT tuning control and slow temperature control to facilitate offset frequency locking to the transmitter, 3) a 2GHz p-i-n InGaAs detector with a quantum efficiency of 70% and a linear range greater than 5 mW of optical power, 4) wide bandwidth, low noise, RF preamplifier and amplifiers, and 5) high power AR coated optics.

The beam expander has a standard aluminum reflective coating with a protective SiO overcoat. This coating is sufficient assuming a long pulse, $10\mu s$ format; however, for an 8ns pulse the power level (1.5 GW/cm^2) exceeds the damage threshold of aluminum. If this expander is to be used as a short pulse transmitter, the secondary mirror must be recoated with a high power HR coating. Although it would be desirable to have a broad band coating, none can be obtained for these high power specifications. High power, high reflective dielectrics can easily handle the damage threshold for single wavelength operation. However, these power levels push the state of the art for high power harmonic HR coatings. CREOL has successfully tested a witness sample of such a harmonic HR coating and will have both the secondary and primary stripped and recoated with this dielectric.

All other components of the coherent laser radar were tested and performed well within the manufacturer's specifications. Of particular interest to a coherent laser radar is the upper limit of
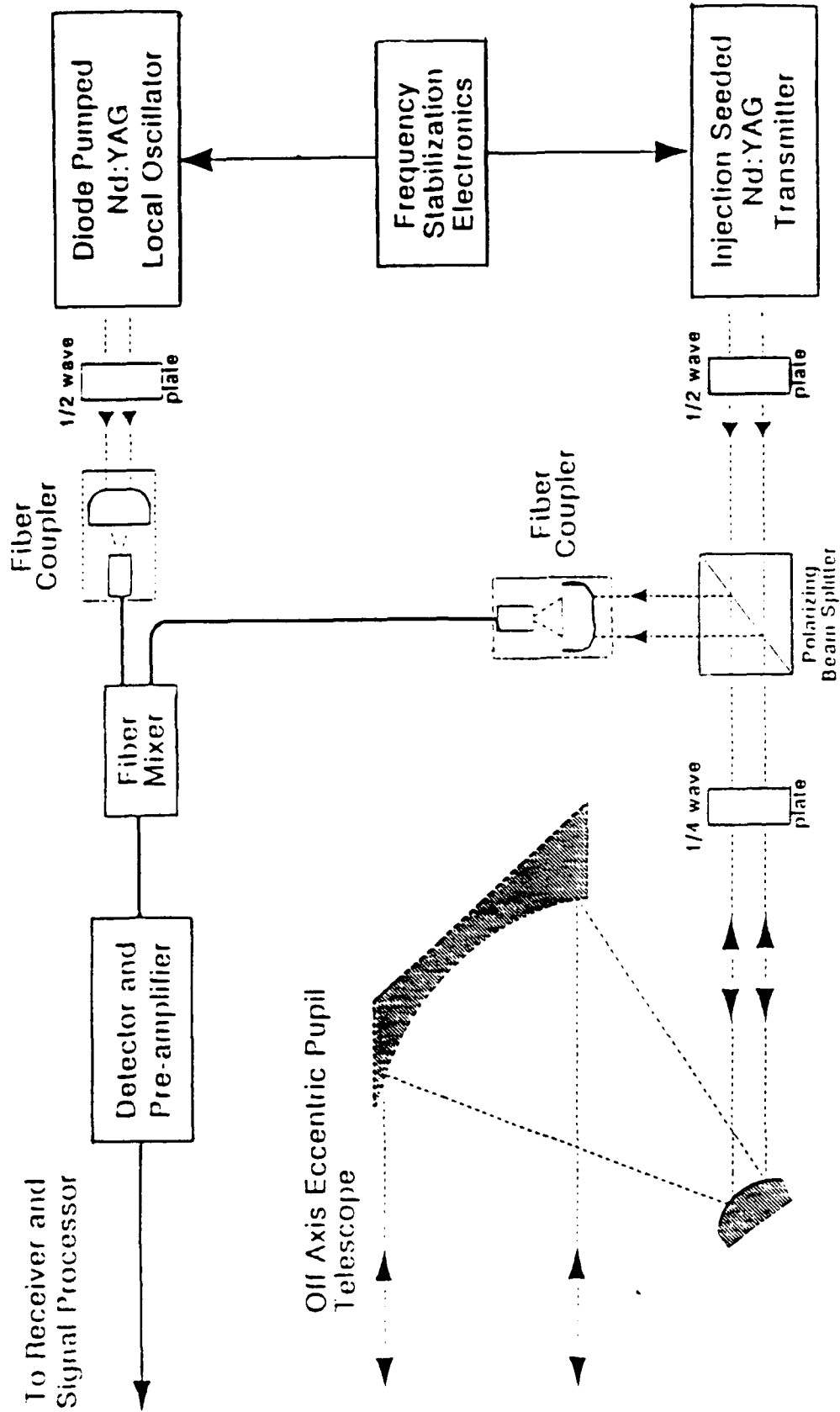
Figure 2-1 Coherent Laser Radar Block Diagram

COHERENT 1.06 MICRON LADAR SCHEMATIC

6

the detector's linear range, which for the Epitax ETX 100T was found to be well above 5 mW of optical power. Since the incoherent ladar program has superseded the coherent program, integration and testing of these components have been delayed.

2.3 Continuing Research

CREOL is currently operating under a follow-on ONR grant. Under this grant CREOL will perform the following activities given in order of priority: 1) perform laser characterization and modifications, 2) continue the development of an incoherent laser radar system, 3) conduct initial ISTEF incoherent ladar experiments, 4) train the ISTEF personnel, 5) develop and exercise an in-house coherent one micron laser radar simulation capability, 6) convert the incoherent one micron ladar to a coherent one micron ladar, and 7) transfer the technologies developed in the coherent ladar simulation lab into the ISTEF coherent ladar testbed.

2.3.1 Laser Characterization and Modifications

Laser characterization is a critical step in the design of a ladar system. A characterization of both the near and far field profiles is critical. The near-field profile must be carefully analyzed to determine the peak intensity levels of localized hot spots. The far-field profile is critical, as this parameter determines the beam divergence, energy transfer efficiency, and beam shape as needed to invert reflectivity data.

It has been determined that the laser (a Continuum NY82-20) suffers from excessive divergence in the green and residual IR beams. Even though the manufacturer did not spec the beam quality output of the doubler, from discussions with a the laser designer, CREOL has determined that the system is behaving abnormally. CREOL is currently investigating this problem and making the necessary modifications to correct the system.

2.3.2 One Micron Incoherent Ladar Development

CREOL is currently (July 1991) completing the design of the transmitter and receiver of a field hardened one micron incoherent ladar. The details of this design will be forthcoming in a final report to be submitted in January of 1992. Remaining tasks include: final system assembly, detector (APD) testing and calibration, and range gate electronics design.

2.3.3 ISTEF Incoherent Ladar Experiments

CREOL will conduct initial ladar experiments at ISTEF to verify system operation and calibration. These experiments will include, in chronological order: 1) tests at the ISTEF 1 km range against stationary targets, 2) low altitude satellite tests (assuming approval is obtained), and 3) tests against targets of opportunity including both plume and hard-bodies.

2.3.4 ISTEF Personnel Training

CREOL will ensure that the appropriate ISTEF (site contractor) personnel are briefed and trained for system operation. This training will occur simultaneously with the initial tests mentioned above. After system handoff, test, and training, CREOL will be on call for further ISTEF support.

2.3.5 One Micron Ladar Simulation Laboratory

CREOL is beginning the development of a one micron ladar simulation laboratory. This laboratory will include both a computer simulation capability as well as an analog simulation laboratory. Areas of research interest include: 1) innovative receiver structures and signal processing to improve heterodyne efficiency in the presence of atmospheric turbulence, 2) innovative techniques to harden a coherent transceiver, 3) measurement and prediction of ISTEF atmospheric extinction conditions and calibration techniques, 4) laser radar cross-section analysis and measurement, and 5) bidirectional laser reflectance data.

2.3.6 Coherent One Micron Ladar Development

After the successful completion of the plume backscatter and autodyne experiments, the Nd:YAG ladar is scheduled to be reconfigured into a coherent laser radar system. This ladar will be a single frequency, 1064 nm, employing a 4" monostatic transceiver and operated in an "on-the-mount" configuration on the ISTEF Contraves Kineto mount. In the initial configuration, this ladar will utilize a single InGaAs p-i-n detector and a variable offset local oscillator, with a conventional beam splitter for local oscillator mixing.

2.3.7 Technology Transfer

CREOL anticipates modifying the initial coherent laser radar configuration, described above, to employ an array receiver and fiber optic coupling technology developed in the $1.06\mu m$ Ladar Simulation Laboratory at CREOL. This technology will allow larger aperture receivers to be

employed in the coherent ladar program, while maintaining heterodyne efficiency and increasing the heterodyne carrier to noise ratio. Current plans are to employ the 4"/20" optic incorporated in the Coude' feed mount, which will be used in the incoherent Nd:YAG experiments.

2.3.8 Program Schedule

Below is an estimated time schedule for the continued research efforts to be conducted at CREOL.

CREOL Nd:YAG Program Time Schedule

	1991			1992		
	3	6	9	12	3	6
Incoherent System Design	*	*	*			
Incoherent Experiments			*	*	*	
ISTEF Personnel Training			*			
Simulation Lab			*	*	*	*
Coherent Ladar Development				*	*	*
Coherent Experiments						*
Coherent Technology Transfer						*

3. ATMOSPHERIC SEEING MEASUREMENTS

Arthur R. Weeks, Ph.D.
Image Processing Laboratory/Computer Engineering

3.1 Background

The purpose of this task was for CREOL to provide ISTEF with a measurement technique by which "atmospheric seeing" could be quantified. "Atmospheric seeing" is defined as the degradation of an image by the atmosphere due to atmospheric turbulence. Since all of the images completed and proposed at ISTEF require long range imaging through the atmosphere, it is of primary importance that the effects of the atmosphere be quantitatively defined.

It is important to realize that the atmosphere degrades an image in two ways. The first, known as scintillation, is the result of turbulence in the upper atmosphere (>3 km) and causes the amplitude of an image to fluctuate with time. The second phenomenon, known as seeing, tends to degrade an image by blurring, which results from turbulence just above the telescope. The type of imaging required at ISTEF is typically through a vertical path in the atmosphere in which the effects of image degradation are considered the most important. The reason that seeing is the predominant degradation effect is that most of the atmosphere is contained within the first 3 km distance above the earth. Another important fact is that since scintillation effects are due to atmospheric turbulence above 3 km while seeing degradation is due to atmospheric turbulence below 3 km, there is very little correlation between the two degradations.

Seeing degradation will affect an image in two ways: first, it will tend to make an object within an image move randomly about a point, and second it will result in blurring of the object. How these two affect an image depends on the integration time of the imaging system. For long time exposures, image motion integrates to a time-averaged image that is blurred. Blurring is due to many correlation cells (seeing disks) that appear at the entrance aperture of a large telescope system.

9

Each seeing disk effectively images into the focal plane of a telescope an image that is slightly displaced from other seeing disks. The sum of all of these seeing disks is the observed image, which is blurred.

In Figure 3-1, the aperture of the telescope is such that the three seeing disks image an object into the focal plane of the telescope at different locations. The net effect is a blurring of the object. If the telescope aperture is reduced in size so that only one seeing disk images through the telescope, there will be only one image that will be moving randomly about a fixed central point. The random motion is due to movement of the seeing disk with time. This is why when very short exposures are taken of images observed through the atmosphere, near diffraction limited results can be obtained. A short timed exposure freezes the image motion so that effectively only one image is obtained. On the other hand, long integration times integrate this image motion into a blurred unresolved image.

3.2 Theory

Figure 3-1 shows that the size of the seeing disk determines the effective aperture size needed for a telescope system. Hence by measuring the size of the seeing disk at various observation sites, relative seeing performance can be made (Ref. 2, 4, 5). The parameter used to measure the seeing disk size is known as the Fried parameter, r_o (Ref. 1).

To measure the Fried parameter, a telescope system images an unresolvable star, and the effective size of star is determined, assuring the model for the star is a point source.

The maximum theoretical angular resolution Θ of a telescope is given by $\Theta = 1.2 \, \lambda/D$, where λ is the wavelength of light assumed to be in the middle of the visible band and D is the diameter of the telescope. For typical values, D = 11 inch and $\lambda = 0.5 \, \mu m$, $\Theta = 1.78 \, \mu rad$. This value is about a factor of 5 smaller than the minimum angular spread of the star's image by the atmosphere. A typical spread of the atmosphere is on the order of 10 μrad, reducing the effective diameter of the telescope to approximately 2 inches. This would tend to indicate that a 20 inch telescope yields the same resolution as a 2 inch telescope.

This effective diameter of the telescope as mentioned above can be determined from Fried's parameter, r_o, which is a measure of the spatial coherence of the EM wave due to turbulence. The intensity pattern at the image plane of the telescope due to seeing effects is very similar to a Gaussian shape. To find r_o, the Modulation Transfer Function (MTF) of the atmosphere must be found. The MTF of the image is defined as the Fourier transform of the image of a point source,
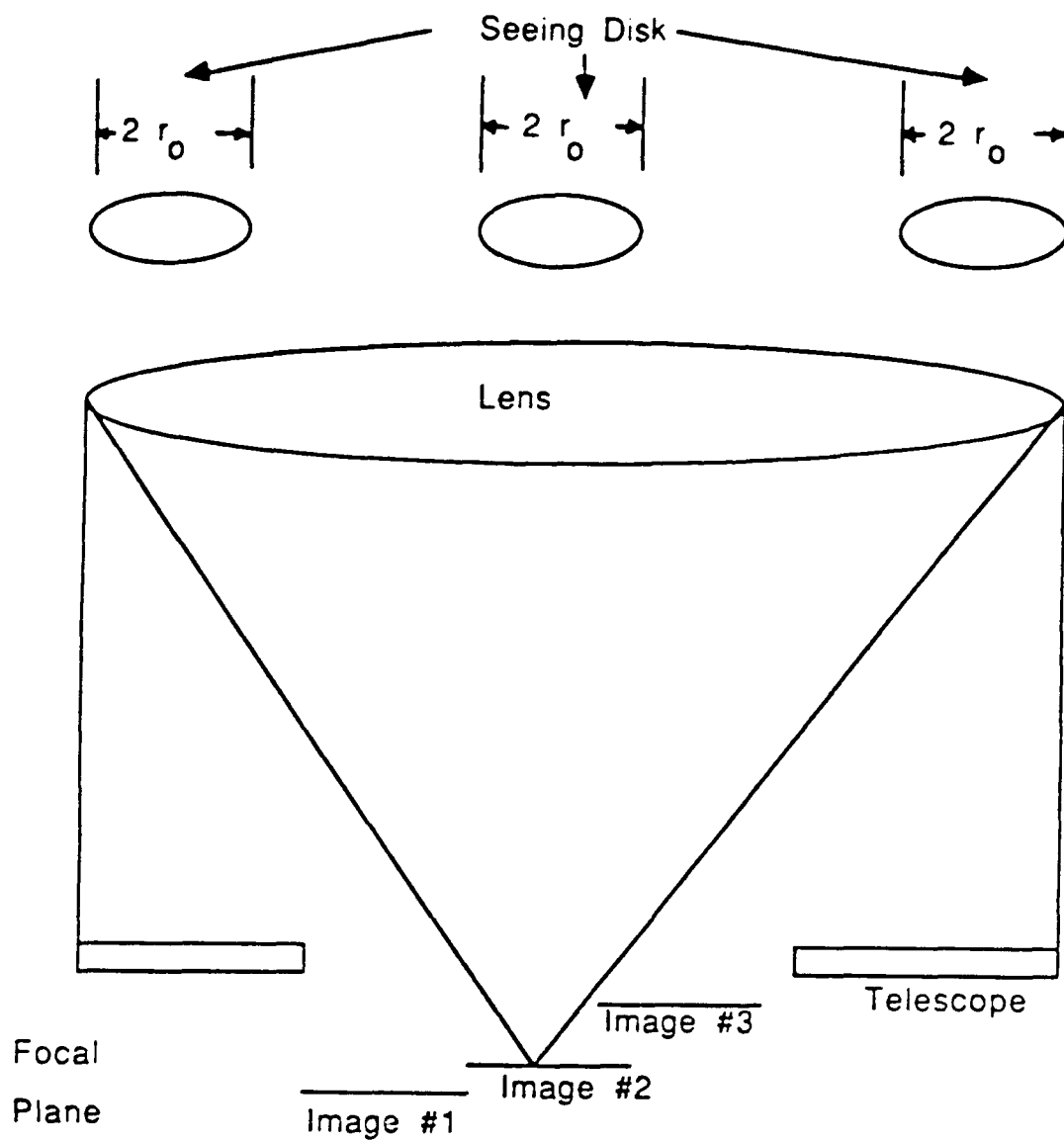
Figure 3-1 Typical Telescope System Depicting Multiple Seeing Disks

at the image plane of the telescope. The total MTF of a star that is imaged by a telescope is given by

$$MTF_i - (MTF_{st})(MTF_a)(MTF_t). \qquad (3\text{-}1)$$

Where MTF_i, is the MTF of the image; MTF_{st}, is the MTF of the star; MTF_a, is the MTF of the atmosphere; and MTF_t, is the MTF of the telescope. For a high quality telescope, its MTF is spatially flat (i.e. a constant). A star which is unresolvable by the telescope, has a spatially flat MTF as well. Thus, the total MTF of the imaging system depends only on the atmospheric MTF, which is given by

$$MTF_a(\rho) - e^{-3.44\,(\rho/r_o)^{5/3}}. \qquad (3\text{-}2)$$

Where $\rho = \lambda f\nu$; λ, is the wavelength of light; f, is the focal length of telescope; and ν, is the spatial frequency in lines/nm.

Since the MTF of the image is nearly Gaussian in shape (i.e., 5/3 instead of 2), the image intensity distribution will also look very similar to a Gaussian. The larger the measured value of r_o, the better the seeing conditions are.

The determination of r_o can be used to find optimum locations or sites to locate observatories. Experimental measurements can be made with known diameter stars to determine the value of r_o for various locations. In addition, the effects of humidity, temperature, and such things as the height of the telescope above the ground on r_o can be determined.

To measure r_o directly, the MTF of the image is obtained and the $e^{-3.44}$ point is determined; unfortunately this measurement point is located within the low signal-to-noise portion of the MTF curve, far out in the tails of the measured intensity distribution. Tutomirski and Yura proposed using (Ref. 3)

$$MTF_a(\rho) - e^{-(\rho/\rho_o)^{5/3}}, \qquad (3\text{-}3)$$

where $r_o = 2.1\rho_o$ to find the e^{-1} point. This leads to more accurate results, since the measurement point is now located at the e^{-1} point instead of the $e^{-3.44}$ point.

3.3 Experiment

Figure 3-2 shows the experimental setup used at ISTEF to measure r_o. The experimental setup contained a Questar telescope, a Sony CCD camera, the Contraves tracker system located at ISTEF, and an IBM PC clone with a Data Translation imaging system. The Questar telescope is a Cassagranian telescope with a 12 inch aperture and 180 inch focal length. Attached to the telescope is the Sony CCD camera with a horizontal and vertical pixel resolution, respectively, of 23 by 13.4 μm. The video output of the camera is next digitized by the IBM PC frame grabber system. This system provides the capability of averaging at a rate of 8 frames/second up to 256 frames.

The tracker is used to bring the image of the desired star into the FOV of the telescope/camera imaging system. Once in the FOV of the system, the tracker is locked into the star and tracks it. When data are to be taken, the star is moved to the upper left corner of the viewing system, by applying an offset to the tracker system. The tracker is then turned off, and the star is allowed to drift freely through the FOV of the telescope. During this time the IBM PC system acquires a set of integrated frames. Turning off the tracking system guarantees that the effects of tracker jitter will be completely eliminated from influencing the experimental data.

Since the video system/frame grabber is an RS-170 8 bit system, the total integration time in which data were acquired was set to 20 frames. This reduces the effect of quantization noise when computing r_o from the acquired data.

With this setup, the procedure required to obtain the desired image data is (see Appendix A for more details):

1. Set up equipment as shown in Figure 3-2.
2. Make sure that all video lines are properly terminated. This reduces video smearing.
3. Use the IBM PC with its frame grabber boards to acquire 20 frames of data per run.
4. Save these data on floppy disk for further analysis.

Performing these steps will produce a digitized image that contains an integration of the motion of the star as it moves through the FOV of the telescope.

3.4 Results

The combined camera and telescope system will image the star onto the CCD with a diameter D with the diameter being proportional to the focal length of the telescope. The total
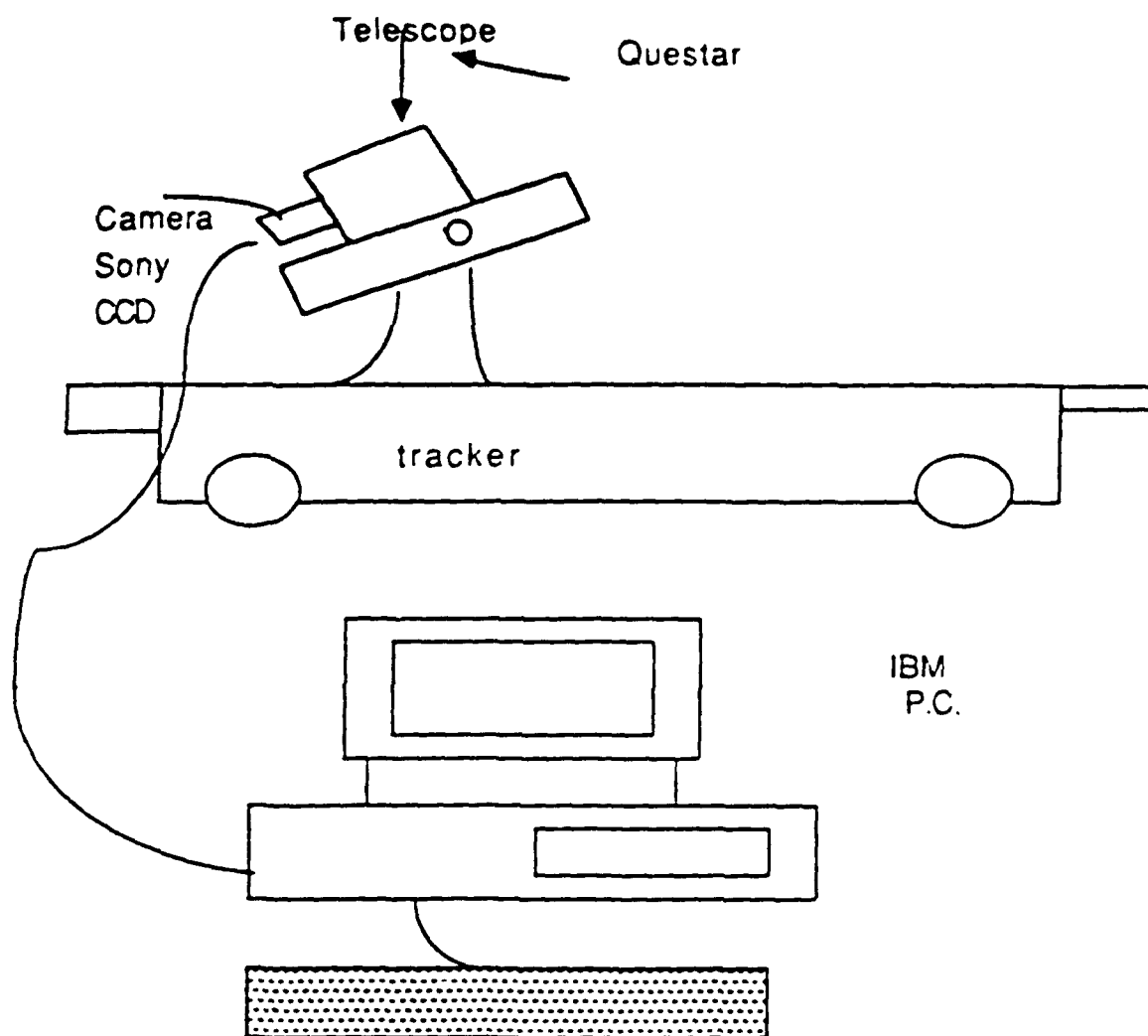
Figure 3-2 CREOL Designed ISTEF Seeing Measurement Apparatus

diameter of the image on the CCD detector will be

$$D - f\,\Theta \qquad\qquad (3\text{-}4)$$

where Θ is the angular width of the star's line spread function.

For Θ of about 2 arcseconds of seeing and $f = 180$ inches, the size of the star at the image plane will be 45 μm. This is about 2-3 pixels of width.

Since a simple experimental setup is required, the use of no tracker reduces the complications caused by vibrations from the telescope's motion, which blurs the time averaged line spread function even more. The resulting image on the CCD camera will be a line produced by the star as it traverses the telescope's FOV and averaged by the CCD camera. The transverse width of this line will be the one-dimensional line spread function.

The averaged line spread function is obtained by averaging several perpendicular slices. The total averaging time required to produce an averaged line spread function is on the order of tenths of second. To obtain the one-dimensional line spread function, several transverse slices are made through the horizontal star streak, and then these slices are averaged. Before actually averaging the slices, to remove any low-frequency vibrations that might be due to wind vibrations on the telescope, the centroid for each slice is computed. Next, each slice is aligned to its centroid and averaged with all the other slices to yield the time-averaged one-dimensional line spread function.

To obtain the MTF of the atmosphere, the Fourier transform of the one-dimensional line spread function is computed and the location of the e^{-1} point is determined. Then, with the help of Eqn. 3-3, r_o can be computed. It should be mentioned that, if the aperture of the telescope is on the order of r_o, the MTF of the atmosphere must be corrected to include the effects of the telescope. This is done by dividing the measured MTF by the MTF of the telescope. For the experimental setup utilized at ISTEF, the telescope MTF was considered constant, since on a night of very good seeing r_o was typically smaller than 150 mm, which is smaller than the diameter of the telescope. r_o can then be determined by simply measuring the e^{-1} points of the line spread function and computing r_o directly. This step eliminates the need to use a discrete fourier transform to compute r_o making the data analysis simpler (Refs. 2, 4, 5).

On one particular night, the seeing was extremely good. The quality of the images of the stars produced exceptional good quality even to the naked eye. The star Alpha Lyrae was observed, which was about 15 degrees from the zenith.

16

A curve fit of this line spread function to a Gaussian curve is

$$L(x) = 140e^{-(x-288)^{2/11}},$$ (3-5)

from which we obtain

$$\sigma = \sqrt{11}\, d,$$ (3-6)

where $d = 23$ μm. Taking the Fourier transform of Eqn. 3-5 and equating it to Eqn. 3-3 yields

$$\rho_o = 0.67 \frac{\lambda f}{d}$$ (3-7)

or

$$r_o = 1.41 \frac{\lambda f}{d}.$$ (3-8)

Assuming λ is in the middle of the visible spectrum, $\lambda = 0.5$ μm, $f = 180$ inches, and $d = 23$ μm, r_o is given by 140.1 mm.

To compute the effective angular resolution, the diffraction equation ($\Theta = 1.22 \lambda/d$) is used for the case $d = r_o$, which yields $\Theta = 1$ arcsec, considered to be very good seeing.

3.5 Conclusion

Data were taken to show that, using a simple experimental technique of a telescope and a video camera, seeing measurements can be easily made. Using a portable tracker, which is now available at ISTEF, this equipment setup can be easily made portable, so that remote site testing can be done.

3.6 Appendix 3-A

Equipment Procedures:

1. Mount the Questar telescope to the Contraves tracker mount.
2. Attach the Sony CCD camera to the Questar telescope.
3. Attach the Motorola computer to the Contraves tracker.
4. Install the data translation boards in the IBM PC clone.

5. Connect the video cables from the Sony CCD camera to the IBM PC computer and to a video monitor for viewing.

6. Terminate the video cables correctly.

7. Run the IRIS program in the PC to display and acquire the video images.

8. Acquire the desired star with the tracker.

9. Offset the star in the video display to the top of the screen.

10. Turn the tracker off.

11. Acquire the image data for X frames.

12. Save the image data to disk.

13. Repeat step 8 until done.

3.7 References

1. D. L. Fried, "Optical Resolution Through a Randomly Inhomogenous Medium for Very Long and Short Exposures," *JOSA* 56, pp. 1372-1379, 1966.

2. D. L. Walters, D. L. Favier, and J. R. Hines, "Vertical Path Atmospheric MTF Measurements," *JOSA* 69, pp. 828-837, 1979.

3. R. F. Lutomirski and H. T. Yura, "Wave Structure Function and Mutual Coherence Function of an Optical Wave in a Turbulent Atmospheric," *JOSA* 61, pp. 481-487, 1971.

4. D. L. Walter, "Atmospheric Modulation Transfer Function for Desert and Mountain Locations: r_o Measurements.," *JOSA* 71, 406-409, 1981.

5. D. L. Walters K. E. Kunkel, "Atmospheric Modulation Transfer Function for Desert and Mountain Locations: the Atmospheric Effects on r_o.," *JOSA* 71, pp 397-405, 1981.

18

4. ATMOSPHERIC INDUCED
ENHANCED BACKSCATTER CHARACTERIZATION

Ron Phillips, Ph.D.
Wave Propagation Laboratory/CREOL

4.1 Background

The goal of this task was to investigate the scattering of an optical wave due to the double passage through atmospheric turbulence known as the enhanced backscatter effect. The investigation was concerned with developing an understanding of the physical phenomenon via both numerical and laboratory experiments. Possible applications for tracking targets from the ISTEF facility were to be considered.

To extract diffraction limited information an adaptive optical system operates as a closed loop system, whereby an error signal of a physical observable is minimized. If an optical system were to operate in an open loop mode and still extract diffraction limited information, a most sophisticated understanding of the propagation process would be required. A closed loop system simply minimizes an error by physically changing the optical system such as by a deformable mirror. An open loop system would be a much simpler hardware system but would require signal processing, thereby putting the burden of the information extraction on computation and NOT on hardware. Usually this is a less expensive solution, since electronic hardware is less expensive than optical hardware. The open loop approach is model dependent and requires a simple yet sophisticated mathematical model if the information is to be extracted in real time. Hence, open loop operation of an optical system that can extract diffraction limited information requires a deep understanding of the propagation physics.

There are two basic architectures for laser beam systems for tracking and imaging of targets. The bi-static system is an architecture with the laser transmitter aperture separate from the receiver aperture. The laser beam path can be assumed to be through two independent turbulent propagation paths. The second architecture is a mono-static system, in which the laser transmitter

19

and receiver share the same output aperture. Hence the transmitter and receiver have coaxial fields of view. The propagation path of the laser beam then passes twice through the same turbulence (assuming slow evolution of the turbulence). The scattering of the returned wave is then correlated with the transmitted wave. This correlation permits a reciprocity of the passage of a wave through any scattering path. In other words, two rays can pass through any scattering path in opposite directions and emerge in phase with one another. It is the presence of correlation that may be exploited to extract diffraction limited information from the returned beam.

The physical genesis of the phenomenon of enhanced backscatter (EBS) is reciprocity of electromagnetic wave propagation. If a transmitted ray is reflected from the target back to the receiver, another ray can take the same path but in the reverse direction. The two rays will arrive at the receiver in phase with one another because they both traversed the same inhomogeneities, albeit in reverse order.

Depending upon the specifics of the wave, i.e., plane, spherical, or beam wave, the double pass scattering phenomenon has the following characteristics:

1. An increase in the fluctuations of the intensity at the transmitter aperture plane;

2. An increase in the fluctuations of the phase of the wave;

3. A decrease in the transverse spatial phase of the wave;

4. A retention of diffraction limited information about the reflecting target.

4.2 Analysis of Enhanced Backscatter

The essence of EBS can be understood by considering a uniform plane wave passing through a random phase screen and being reflected back onto itself. Here we use a simple phase screen as a model for the turbulent atmosphere and a ray model for the wave. For a uniform plane wave incident on the screen, the rays are all parallel and propagating in the direction of incidence. The medium disperses the rays over a variety of directions. The rays then propagate onto the target and are reflected back through the same screen. The rays emerging from the screen along reciprocal paths will emerge in phase in the direction of incidence of the incoming wave. Although the absolute phase of the scattered wave will fluctuate, in the direction of the incidence the scattered waves will be in phase because the rays traverse the same refractive inhomogeneities but in opposite directions. In Figure 4-1, the rays E_1 and E_4 are in phase and E_2 and E_3 are in phase, but E_1 and E_2 are not in phase, nor are E_3 and E_4, because these rays do not have reciprocal paths. Suppose we now place a collection lens behind the aperture and an array detector behind the lens. If the
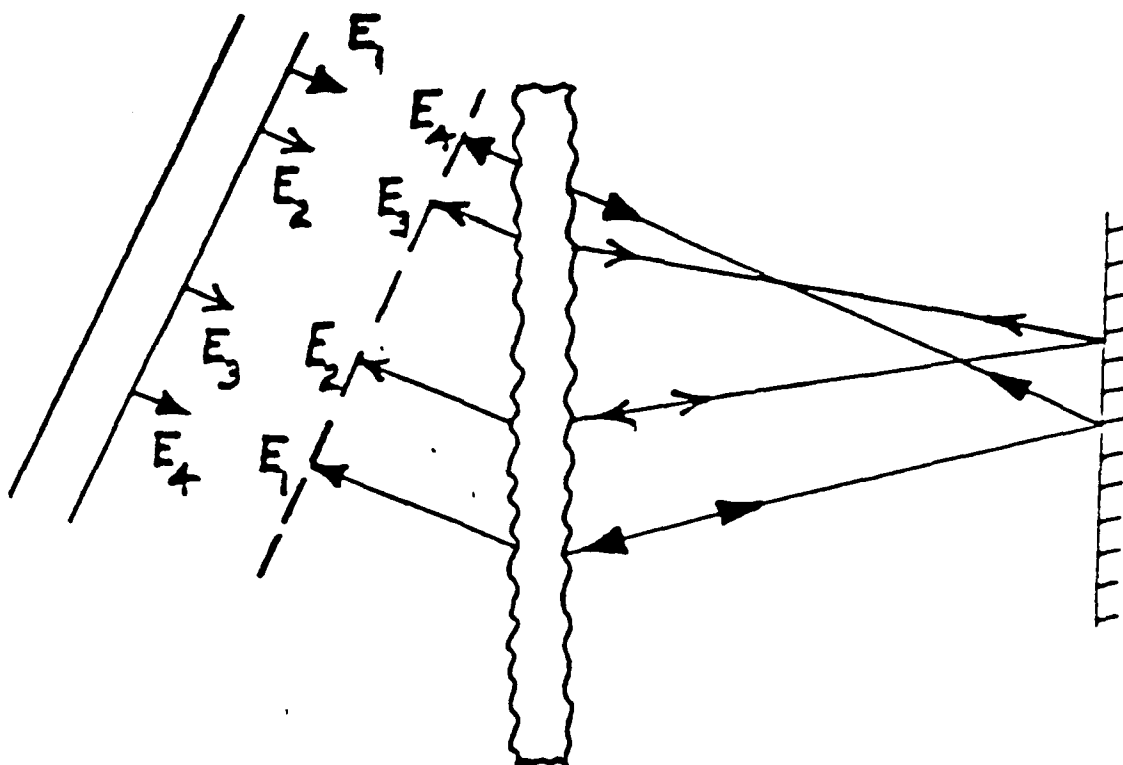
Figure 4-1. Schematic of infinite uniform plane wave incident on a phase screen

array detector is in the focal plane of the lens, it will be in the far field of the aperture. The detected double pass coherent wave will appear as a sharp intensity peak in the focal plane. The location of this peak relative to the entire received signal will give the location of the target to the resolution of the optical system.

4.3 Experimental Results

Figure 4-2. is a series of photographs of the intensity fluctuations of a laser beam after passing through a random phase screen generated by warm air turbulence. Figure 4-2a is just beyond the screen, Figure 4-2b is at the "focus" of the screen, and Figure 4-2c is in the far field of the screen. Figure 4-3 shows a TV image of a plane wave after passing twice through a random phase screen in a laboratory experiment. Figure 4-3a shows the characteristic speckle. Figure 4-3b is the TV image of the multi-frame averaging automatically performed by the TV camera by rapidly moving the random phase screen faster than the camera could time resolve the moving speckle pattern. The bright spot is the enhanced backscatter due to the double passage.

Figure 4-4 is a photograph of the laser intensity fluctuations after propagating a distance of 1000 meters on an outdoor range. The aperture of the collecting lens for the camera was smaller than the beam diameter.

Joint experiments were performed with the Royal Signals and Radar Establishment of the British Ministry of Defense in Malvern England. EBS experiments have been performed on a 1,000 meter outdoor range (see Figure 4-5a). A HeNe laser beam was pointed down range to a retro-reflector. The returned wave was detected by a CCD TV camera located in the focal plane of a collection lens. The TV images were recorded on a VCR. The TV recorded images were played into a frame grabber and 128 frames averaged together. The result is shown in Figure 4-5b. The angular resolution of the position of the target (retro-reflector) due to turbulence is qualitatively defined by the smeared signal. The EBS signal clearly shows the location of the target to within the diffraction limit of the collection optics. The picture shows an approximate factor of 5 increase in angular resolution over the turbulence reduced resolution.

4.4 Conclusions

The results of this study show that the enhanced backscatter of the double passage of a wave through the atmosphere can be used to obtain diffraction limited information about a target. This was shown by processing data from both laboratory and outdoor experiments.
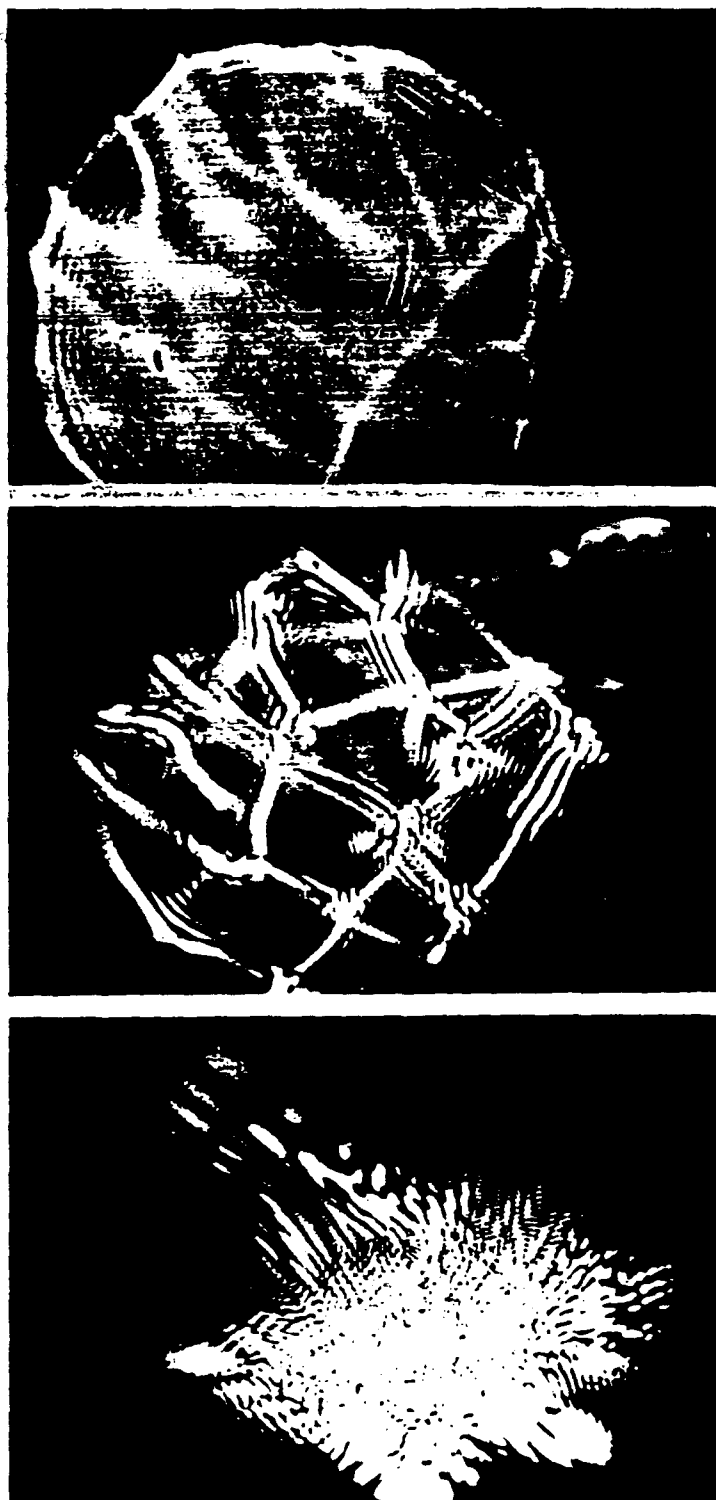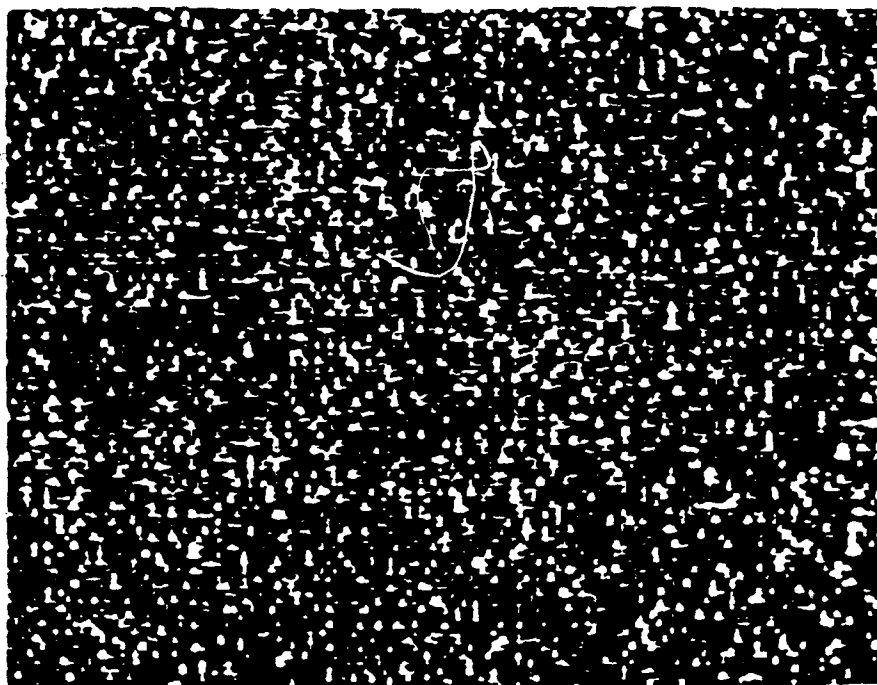
Figure 4-2. The top photo is the intensity fluctuation of a laser beam just beyond the random phase screen. The middle photo is the beam fluctuations in the "focus" region of the screen. The lower photo in the far-field of the screen showing the Gaussian like fluctuations of the beam.
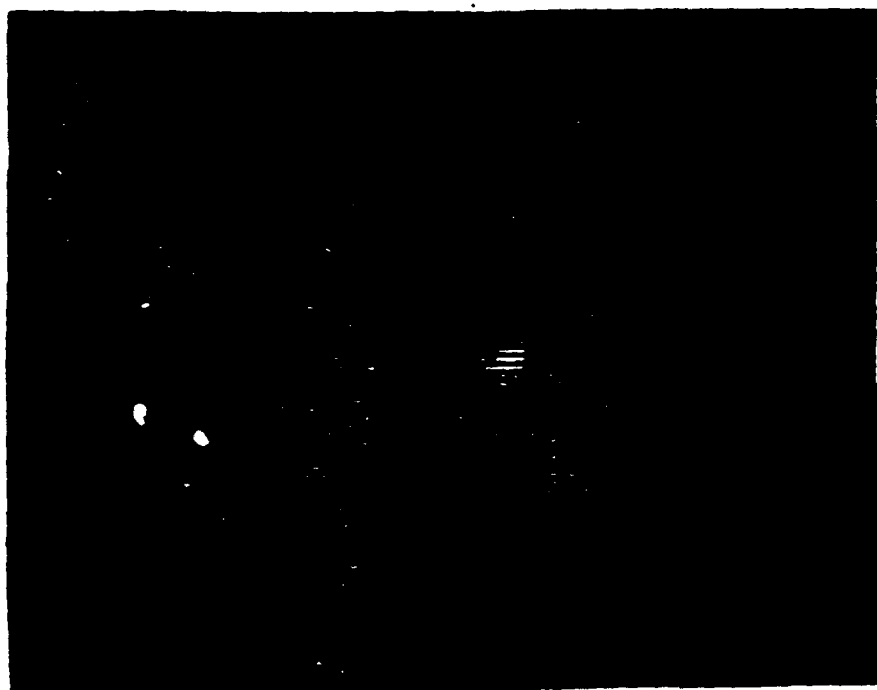
24

(a)

Figure 4-3. This is a TV image of a beam after passing twice through a phase screen. Figure 4-3a is the speckle without processing the signal. Figure 4-3b shows the EBS signal after averaging many TV frames.

Figure 4-4. A photo showing typical intensity fluctuations of a beam after a single pass through 1000 meters along an out door range.
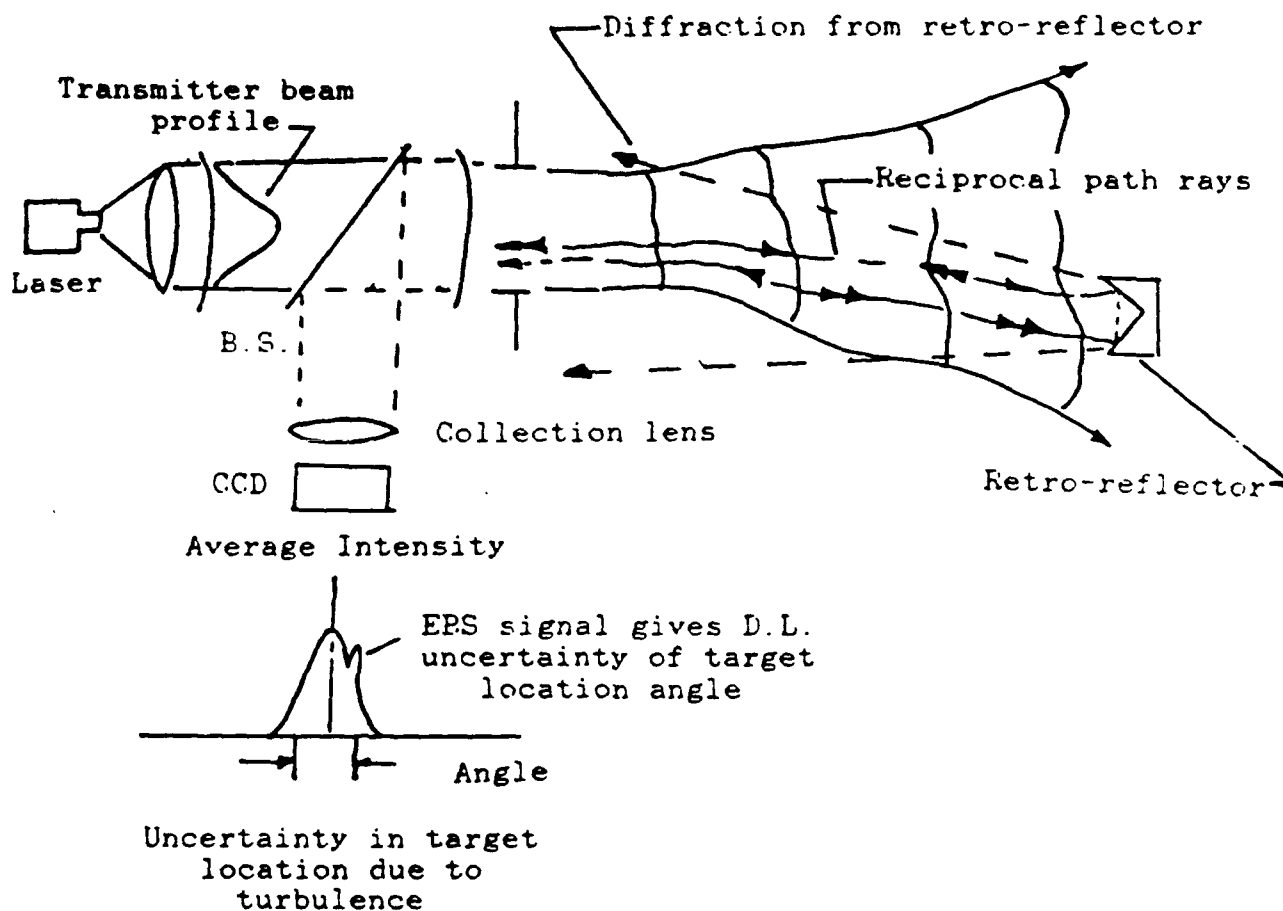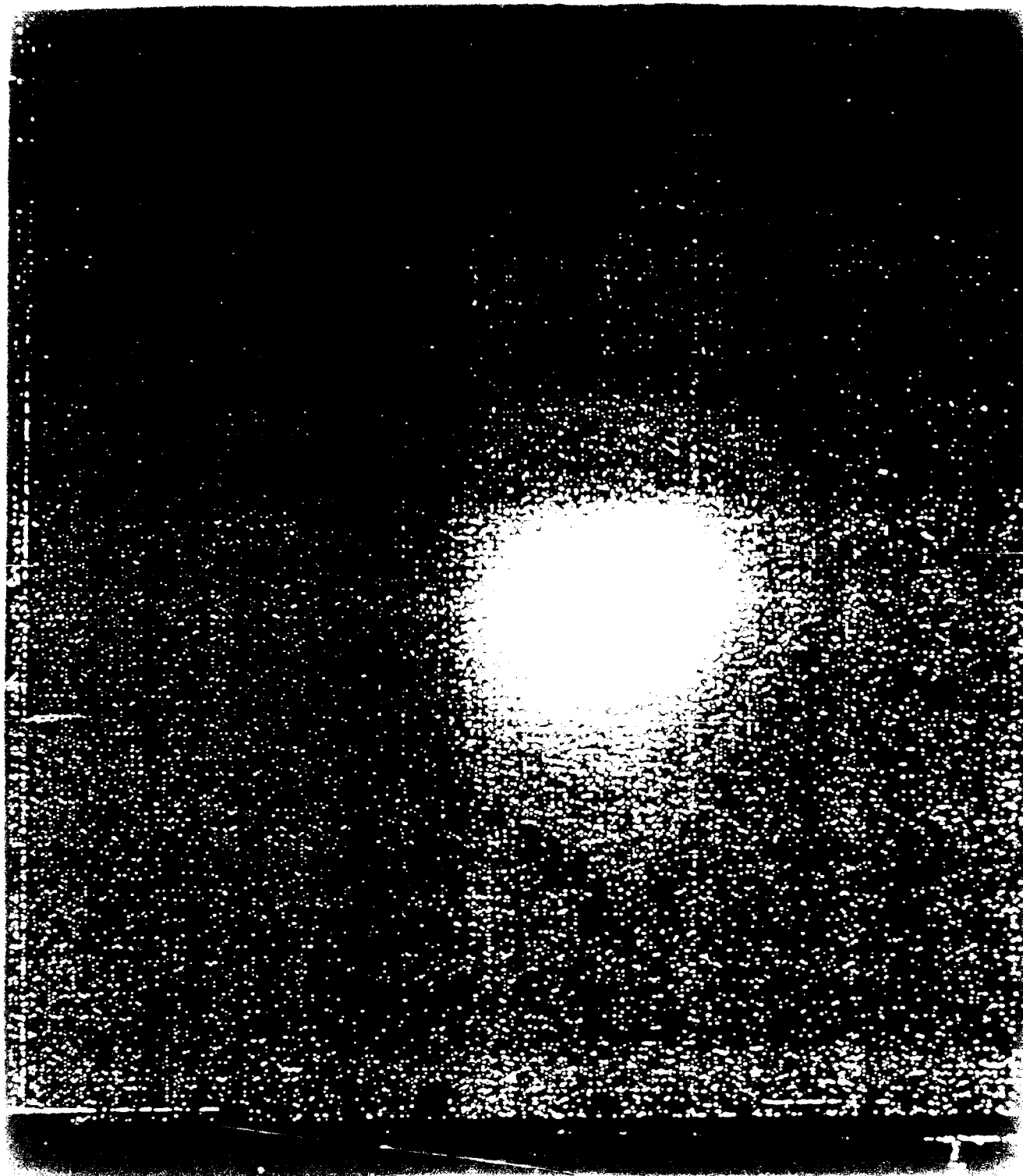
Figure 4-5a. A schematic of a mono-static transmitter/receiver. The EBS signal can be extracted from the focal plane of receiving collection lens by processing the detected signal from a CCD array in the focal plane.

28

4.5 Appendix 4-A

Simulation of enhanced backscatter by a phase screen

Gisele Welch and Ronald Phillips

Center for Research in Electro-Optics and Lasers, University of Central Florida, Orlando, Florida 32816

A simulation was constructed, and numerical experiments were conducted, of optical-wave double-pass propagation through a phase screen. The phase screen had a Gaussian phase fluctuation with a Kolmogorov power-law spatial spectrum. The results are compared with a theoretical model developed for a similar scattering process but for a phase screen with a Gaussian spatial spectrum.

1. INTRODUCTION

There has been a vested interest in the study of waves reflected or scattered backward through a random inhomogeneous medium. Both theoretical and experimental work has been conducted in this area most recently by Jakeman,[1] Jakeman et al.,[2] Tapster et al.,[3] Tatarski,[4] and Espipov and Zosemov.[5] The interest comes about because of the areas of research that can be developed with this phenomenon. These areas include imaging, remote sensing, and the study of sound-wave propagation through the ocean. This enhancement might be used to track objects in the atmosphere. Furthermore, this phenomenon might be used to find the optical axis in a complex system.

The study of wave propagation through random media follows the analysis that, as a wave passes through statistically independent phase screens, the screens monotonically increase the scattering effects of the incoming wave. This increase does not occur when a wave is reflected back through the screen that it initially traversed. The effect of double passage on the wave through the same inhomogeneities of the medium is an enhancement of the average intensity of the backward-reflected wave. This effect was observed in a review paper by Kravtsov and Saichev.[6]

A numerical experiment was conducted on the phenomenon of enhanced backscatter. This research was based on a simulation, which was developed by Filice,[7] of interplanetary scintillation of radio waves. This simulation begins with a monochromatic plane wave passing through a random phase screen. The wave is propagated some given distance past the focal plane of the screen and reflected back toward the same screen. The average intensity statistics are studied. Although there are some limitations to simulations of this type, they do provide a useful tool in the analysis of various case studies.[8,9] For instance, the simulation enables us to study different types of mirrors, which are used as reflectors, at various angles and contours. This simulation has been tested and compared with theoretical results published by Jakeman.[1]

Section 2 develops the physical background needed for the analysis, which is followed in Section 3 by theoretical models. Section 4 describes the algorithm used. Section 5 is a brief description of some of the results obtained from the simulation. Finally, in Section 6 we compare these results of the intensity statistics with theoretical outcomes produced by Jakeman.

2. BACKGROUND

When an optical wave passes through a phase screen, the emerging wave has a perturbed spatial phase. As the wave continues to propagate beyond the screen, the wave begins to exhibit amplitude fluctuations if the impressed perturbations are large (variance of phase $\gg 1$). These amplitude fluctuations initially increase with distance; they reach a maximum and then diminish with further increase in distance and eventually approach a saturated value. The distance at which these peak fluctuations occur is referred to as the focus distance. These amplitude fluctuations are due to two different mechanisms, refractive scattering and diffractive scattering. The relative amount of each of these two mechanisms depends on the spatial spectrum of the refractive inhomogeneities and the distance that the wave has propagated beyond the screen. Diffractive scattering dominates the intensity scintillation for scales of the spatial inhomogeneities within the screen of the order of the Fresnel scale, $\sqrt{\lambda z}$, or smaller. Strong refractive inhomogeneities within the phase screen, which are large compared with the Fresnel scale, refractively scatter the wave.[10]

The most-often-used spatial-spectrum models of the refractive inhomogeneities are Gaussian and power law. The Gaussian spectrum has the characteristic of smooth inhomogeneities with a single scale. If the single scale of the Gaussian spectrum is larger than the Fresnel scale, the scattering is due to refractive scattering as is the case close to the phase screen. At long distances from the screen, when the Fresnel scale is large compared with the characteristic scale of the spectrum, the scattering process becomes dominated by diffraction. Hence the scattering processes are somewhat sequential, with the refractive process acting close to the screen and the diffractive process acting at long distances from the screen.

The power-law spectrum has a range of inhomogeneities. Usually the spectrum is assumed to have a smallest and a largest scale, called the inner and outer scales, respectively. Since the power-law spectrum is an inverse power law, the power in the spatial scales decreases as the scale gets smaller, i.e., the spatial wave number increases. At every distance beyond the phase screen where the Fresnel scale lies between the inner and outer scales, i.e., where $\ell_i < \sqrt{\lambda z} < L_o$, there are always some scales of inhomogeneities contributing to both the diffractive- and refractive-scattering processes. The dominant mechanism depends on the relative

strengths of the inhomogeneity scales. At long distances from the screen where the Fresnel scale exceeds the outer scale, diffraction dominates. At distances where the Fresnel scale greatly exceeds the outer scale, i.e., at $\sqrt{\lambda z} \gg L_0$, the contribution to each point in the scattered wave comes from many independent inhomogeneities and from the central limit theorem: the field approaches complex Gaussian. If the screen is spatially homogeneous, the field is circular-complex Gaussian and becomes speckle.

As the wave propagates beyond the phase screen, the transverse spatial correlation diminishes.[11] If a second screen is placed in the path of the wave, the effect that it has on the wave depends on the wave's transverse correlation. When the transverse correlation of the incident wave is larger than the refractive inhomogeneities in the second screen, the inhomogeneities contribute to the phase fluctuations of the wave. For a transverse correlation significantly smaller than the inhomogeneities, the additional effect of the second screen is small.

When a wave passes through a phase screen and is reflected back through the same screen, the effect of the second pass can give rise to a significantly different phenomenon. This phenomenon is an enhancement of the backscattered wave and is due to the refractive fluctuations of the screen being correlated with the wave. There are two separate mechanisms that can give an enhancement to the backscatter: coherent and incoherent. The coherent mechanism is the constructive interference of portions of the reflected wave after it has traversed different refractive inhomogeneities. This is the dominant contributing mechanism to the backscatter when the mirror is placed well beyond the focusing distance of the phase screen. The incoherent mechanism occurs when a portion of the reflected wave passes through the same refractive lenslike inhomogeneity that focused this portion of the wave onto the mirror. The enhancement factor for the incoherent cause may be much larger than that for the coherent case, which is only a factor of 2 above the normal scattering level.

The angular distribution of the backscatter enhancement is very narrow for the coherent process. The enhancement width decreases as the angular distribution of rays increases as a result of the first pass through the phase screen. The width of the enhancement for the incoherent process is greater than that of the coherent process. The width of this contribution is comparable with the width of the specular angular distribution of normal scattering.

3. THEORETICAL MODELS

A wave passes through the scattering medium and is reflected back onto itself. The backscattered wave emerges from the medium into a cone of directions. The emerging waves add together preferentially in the reverse direction of their direction of incidence. For an explanation of the physical scattering process, a ray model is most useful.

For a uniform plane wave incident upon the screen, the rays are all parallel and propagate in the direction of incidence. Within the medium, the rays are dispersed over a variety of random directions. After passing through the phase screen, the scattered rays propagate onto the reflecting surface and are reflected back through the same screen. We assume that, during the time period during which the rays are propagating to the reflector and back, the refractive

inhomogeneities within the screen do not change. We assume that the refractive inhomogeneities change slowly so that subsequent waves and their rays will experience other realizations of the random inhomogeneities.

Consider some particular ray E_1 incident upon the phase screen. Now suppose that E_1 emerges from the second pass through the screen at some new location but pointed in the reverse direction of the incident wave as shown in Fig. 1. At the exit location there is a second ray E_4 entering the phase screen. This second incident ray will traverse the same path as the first ray but in the opposite direction. Ray E_4 will then emerge from the second pass through the screen at the location where E_1 entered the screen but pointed in the opposite direction to E_1. The two rays exchange locations and exit parallel to each other. Because these two rays traversed the same path but in opposite directions, they exit with no phase difference due to the scattering process. In subsequent realizations this pairing of the returning rays will occur whenever any ray can be scattered back into the direction of the incident wave.

If we consider rays emerging from the second pass through the phase screen into directions other than the incident direction, there is no reciprocal path possible. Hence there will be a random phase difference between any two rays in subsequent realization of the screen because each ray will always pass through a different path. Therefore all rays will be incoherent in all other directions but the direction of incidence.

Mathematically we can represent this physical ray model by the following analysis. Let the total field be represented by four component rays such that the total field is

$$E = E_1 + E_2 + E_3 + E_4. \tag{1}$$

The intensity of the field after the double pass is

$$I = |E|^2 = |E_1|^2 + |E_2|^2 + |E_3|^2 + |E_4|^2 + 2E_1E_2 \cos \theta_{12}$$

$$+ 2E_1E_3 \cos \theta_{13} + 2E_1E_4 \cos \theta_{14} + 2E_2E_3 \cos \theta_{23}. \tag{2}$$

Suppose we have a uniform wave so that $I_0 = |E_1|^2 = |E_2|^2 = |E_3|^2 = |E_4|^2$ and therefore

$$I = 4I_0 + 2I_0 \cos \theta_{12} + 2I_0 \cos \theta_{23} + 2I_0 \cos \theta_{13} + 2I_0 \cos \theta_{14}. \tag{3}$$
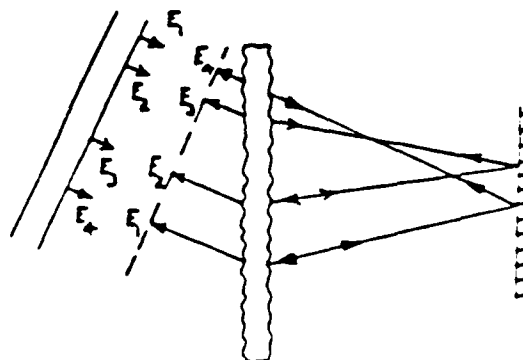

Fig. 1   Schematic of infinite uniform plane-wave incident upon a phase screen

Owing to reciprocal paths, $\theta_{14} = \theta_{23} = 0$, and when we average over many realizations of the phase screen Eq. (3) reduces to

$$\langle I \rangle = 4I_0 + 2I_0 + 2I_0 + 2I_0 \langle \cos \theta_{13} \rangle + 2I_0 \langle \cos \theta_{12} \rangle,$$

$$\langle I \rangle = 4I_0 + (2I_0 + 2I_0), \qquad (4)$$

$$\langle I \rangle = \text{incoherent portion} + \text{coherent portion}, \qquad (5)$$

where $\langle \cos \theta_{12} \rangle = \langle \cos \theta_{13} \rangle = 0$ because, for directions other than that of the incident wave, all phase differences are random.

Recently Jakeman theoretically modeled the scattering that occurs to an optical-beam wave on a double-pass path through the same phase screen. In his analysis he assumed the following:

(1) The induced spatial-phase fluctuation ϕ by the screen is a spatial-Gaussian process with a smoothly varying spatial spectrum.

(2) The mean-square phase fluctuation ϕ_0^2 is much greater than unity, $\phi_0^2 \gg 1$, so that the scattering is strong.

(3) The phase screen is illuminated by a monochromatic Gaussian-beam wave with radius W_0, which is taken to be much larger than the largest diameter of index inhomogeneity. Hence the scattering gives rise to a complex Gaussian spatial process in the far field.

(4) The plane-reflecting mirror is located within the Fresnel region where the illuminated area is much greater than the first Fresnel zone.

(5) The plane mirror is located at a distance z beyond the phase screen within the Fresnel region of the beam such that $z \ll kW_0^2/4$, where $k = 2\pi/\lambda$.

Using these assumptions, Jakeman derived an expression for the far-field intensity distribution of the backscattered wave. He showed that there is an enhancement of the backscattered-light intensity in the direction of the incident beam. For a mirror placed at a distance sufficiently far from the screen, Gaussian speckle will be developed at the mirror. It was shown, for this case, that the average angularly distributed intensity for a Gaussian beam is

$$I(\theta_s) = I_s^{(2)} \exp\left(\frac{-2p^2}{m_0^2}\right)$$

$$\times \left[1 + \frac{W_0^2}{W_0^2 + d^2m_0^2} \exp(-2k^2l^2Q^2)^{1/2} \right]. \qquad (6)$$

where $I_s^{(2)}$ is the peak intensity of the backscattered beam, d is the distance from the screen to the mirror, and m_0 represents the rms value of the sine of the scattering angle of the phase screen.[1] Then the term $d^2m_0^2$ is proportional to the area of the scattering disk at the screen on the second pass. The other parameters are given by

$$l^{-2} = V_1^{-2} + (dm_0)^{-2}, \qquad (7)$$

$$Q = \frac{1}{2}(\sin \theta_s - \sin \theta_i), \quad P = \frac{1}{2}(\sin \theta_s + \sin \theta_i), \qquad (8)$$

where θ_s is the observed scattering angle and θ_i is the angle of incidence.

A reasonable approximation to Eq. (6) for the case of a plane wave would be $W_0 \gg dm_0$ so that

$$I(\theta_s) = I_s^{(2)} \exp\left(\frac{-2p^2}{m_0^2}\right) [1 + \exp(-2k^2l^2Q^2)^{1/2}]. \qquad (9)$$

where l^2 reduces to $(dm_0)^2$. The leading exponential factor describes the intensity angular distribution of the scattered waves owing to two independent phase screens with identical spatial spectra. The exponential term within the brackets describes the intensity-enhancement distribution.

4. SIMULATION ALGORITHM

The wave field is expressed by

$$E(r) = f(r)\exp(-jkr), \qquad (10)$$

where $f(r)$ is the complex amplitude, $k = 2\pi/\lambda$ is the free-space wave number, and $r = (x, y, z)$ is the radius vector. If one assumes propagation in the z direction, the parabolic wave equation becomes

$$2jk\frac{\partial}{\partial z} f(r) + \nabla_t^2 f(r) + 2k^2 n_1(r)f(r, t) = 0, \qquad (11)$$

where $n_1 = n - \langle n \rangle$ is the index of refraction, and $\nabla_t^2 = (\partial^2/\partial x^2) + (\partial^2/\partial y^2)$ is the transverse Laplacian. In free space, Eq. (11) assumes the form

$$2jk\frac{\partial}{\partial z} f(s, z) = -\nabla_t^2 f(s, z), \qquad (12)$$

where $s = (x, y)$ is the two-dimensional spatial variable. The solution of the modified wave equation is found by performing a Fourier transform on both sides, thereby reducing Eq. (12) to an ordinary differential equation

$$\frac{dF(\kappa, z)}{dz} = \frac{j\kappa^2}{2k} F(\kappa, 0), \qquad (13)$$

with spatial frequency $\kappa = (\kappa_x, \kappa_y)$, and the solution given by

$$F(\kappa, z) = F(\kappa, 0)\exp(j\kappa^2z/2k), \qquad (14)$$

where $\exp(j\kappa^2z/2k)$ represents the Fresnel factor. Using Eq. (14) and its inverse, we may transform from the frequency domain to the space domain so as to simplify calculations of phase-screen scattering.

A two-dimensional random phase screen is generated that consists of $M \times N$ equispaced real-phase shifts $\phi(s)$, such that the screen is a member of an ensemble having a specified expected phase spectrum $\Phi_\phi(\kappa)$. The average power spectrum of the phase fluctuations Φ_n from an ensemble of such screens converges to a specified function.

The phase correlation function of the screen is

$$R(s) = \int\int_0^{\Delta z} \langle n_1(z, s_1)n_1(z', s_2)\rangle \, dz dz', \qquad (15)$$

$$R(s) = k^2\Delta z A_n(s_1 - s_2), \qquad (16)$$

where Δz is the width or thickness of the screen. A_n represents the correlation function and may be expressed in terms of the phase spectrum[12]

$$A(s) = 2\pi \int\int_{-\infty}^{\infty} \Phi_n(\kappa_z = 0, \kappa)\exp(j\kappa \cdot s)d\kappa. \qquad (17)$$

Fourier transforming Eq. (16) and using Eq. (17), we find the spectrum of the phase fluctuations to be

$$\Phi_o(\tilde{\kappa}) = 2\pi k^2 \Delta_z \Phi_n(\kappa_z = 0, \tilde{\kappa}). \qquad (18)$$

The discrete phase screen is described by a rectangle with sides $L_x = M\Delta x$ and $L_y = N\Delta y$, where Δx and Δ_y are the spatial-sampling intervals on the screen. (For our study they are taken to be equal.) Pseudorandom $\phi(\tilde{\kappa})$ are generated to satisfy

$$\langle |\phi(\tilde{\kappa})|^2 \rangle = L_x L_y \Phi_o(\tilde{\kappa}), \qquad (19)$$

where $\phi(\tilde{\kappa})$ is the transformed phase and $\Phi_o(\tilde{\kappa})$ is the phase power spectrum. By generating random phase shifts that satisfy Eq. (19) and by taking the two-dimensional discrete Fourier transform (2DFFT), we find that the result is a phase screen that is a desired member of the ensemble. In summary, the phase screens are created by filtering white Gaussian noise to obtain a random field with the desired spectral properties [random phase shift $\phi = (A + jB)/\sqrt{2}$, where A and B are independent random variables that are realizations of a normally distributed random variable that has a variance $\sigma^2 = L_x L_y \Phi_o(\kappa)$]. A power-law spectrum that contains power at all scales was used. Any discrete simulation can contain only a finite range of scales. Thus there are inner and outer scales implicit in any discrete formulation owing to the finite number of sample points and the finite sampling intervals.

The next concern is creating a mirror so that the propagating wave may be reflected back through the same phase screen. This is accomplished through a window acting as a filter that represents the aperture describing a mirror. The mirror was chosen to be some multiple of the sampling interval of the screen. Calculations showed that, as long as the mirror size was greater than $6.38\Delta x \times 6.38\Delta y$, we would be in the Fresnel region of the mirror.

We summarize with the following:

(1) Create random phase shifts $\phi(s)$.
(2) Perform the 2DFFT on $\exp[j\phi(S)]$, which gives the transformed field, $E(\tilde{\kappa}, 0)$.

(3) Multiply by the Fresnel factor, $\exp(j\kappa^2 z/2k)$, for propagation.
(4) Reflect the complex field from the mirror.
(5) Propagate back to the original phase screen by multiplying by the Fresnel factor.
(6) Perform the inverse 2DFFT to obtain the field $E(\tilde{s}, z)$.
(7) Multiply $E(\tilde{s}, z)$ by $\exp[j\phi(S)]$.
(8) Perform two-dimensional discrete Fourier transformation to obtain far-field intensity.

The above algorithm is graphically shown in Fig. 2. This algorithm leads to the study of a wave reflected in the backward direction. In order to see the enhancement, one must study the intensity statistics in the far field, which implies that the Fourier transform of the electric field be taken at the exit plane of the second screen and averaged on an intensity basis.

The simulation has been developed so that all propagation lengths are normalized with respect to the sampling interval Δ_z. Let M be the number of samples such that the spatial-frequency resolution Δ_κ is given by the expression

$$\Delta_\kappa = 2\pi M/\Delta_z. \qquad (20)$$

The power-law spectrum for the phase screen is a function of the strength of turbulence denoted by the parameter T:

$$\Phi_\epsilon(\tilde{\kappa}) = 2\pi T \kappa^n, \qquad (21)$$

where n is the power-spectral index. The strength T may be written as a function of U, which is taken to be the square of the scintillation index:

$$U = -\gamma_\lambda (1 - \alpha/2) \sin\!\left(\frac{\alpha\pi}{4}\right)\!\left(\frac{z}{k}\right)^{n/2-1}.$$

An understanding of the boundaries involved for the screen is obtained from the mutual coherence function:

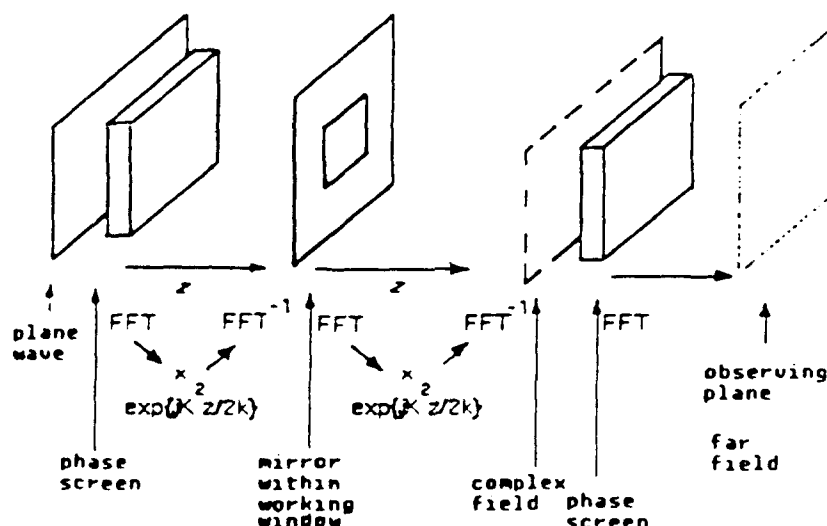$$R(\tilde{s}) = \exp[-\tfrac{1}{2}D(\tilde{s})], \qquad (22)$$

Fig. 2. Schematic of program simulation and computation algorithm.

where $D(s)$, the wave structure function for power-law form, is given by the following expression:

$$D_p(s) = \frac{\left(\frac{\pi}{2}\right)^{\alpha/2-1} U}{(\alpha-2)\Gamma\left(\frac{\alpha}{2}\right)\sin\left(\frac{\alpha\pi}{4}\right)}\left(\frac{s^2}{\lambda z}\right)^{(\alpha-2)/2}, \tag{23}$$

which was derived from the solution to the fourth moment of Eq. (13).[13] Solving for $R(s)$ gives $D(s)$ results in

$$R(s) = \exp\left[-\frac{\left(\frac{\pi}{2}\right)^{\alpha/2-1} U \left(\frac{s^2}{\lambda z}\right)^{(\alpha-2)/2}}{2(\alpha-2)\Gamma\left(\frac{\alpha}{2}\right)\sin\left(\frac{\alpha\pi}{4}\right)}\right]. \tag{24}$$

Hence the larger the U, the narrower $R(s)$ becomes and the more finely sampled the screen must be. Solving for the angular spectrum of plane waves by inverse Fourier transforming $R(s)$, we are able to obtain the parameters needed for the simulation. These include the sampling interval taken to be

$$\Delta y = \sqrt{\lambda z}/16. \tag{25}$$

Hence $Ly = 16(\lambda z)^{1/2}$, and we have $Lx = 2Ly$, where the chosen screen size is 512×256 with an 11/3 spectral index. The above parameters have been validated and compared with other screen sizes by Filice. The parameters that we held constant for our experiment are the aperture width, which is taken to be a $100\Delta x$ by $100\Delta y$ square centered within the observing area; the wavelength, which is taken to be 1 μm; and the distance set to 20 m, which is past the focus distance of the screen.

The testing of the program was conducted by using a deterministic phase shift $\phi = 0$, which resulted in a sinc-function far-field pattern. When a linear phase is inserted, the result is, across the screen, a sinc function shifted by the known amount.

5. RESULTS

The theory of enhanced backscatter relies on the wave's passing through the original screen that it traversed, resulting in a coherent addition of fields. On the other hand when the phase screens are independent, we have an incoherent addition and therefore no enhancement. In Fig. 3 the algorithm was altered so as to produce two independent phase screens. The parameters for this case are 80 realizations with $U = 10$. As predicted, there is only normal scattering with no enhancement, thereby producing another means of validating the program. The next run consists of two identical screens to model the backscatter. This case, shown in Fig. 4, displays the enhancement, which is a factor of 2 above the normal for $U = 10$, 100 realizations. The same case was run for $U = 5$, shown in Fig. 5. As expected, by lowering the strength of turbulence, we widened the enhancement width. The last study conducted for this paper involves the angle of incidence of the incoming wave. We altered the incident angle by 0.012 deg, which resulted in the shifting of the enhancement by the same amount shown in Fig. 6. This run was for 110 realizations with $U = 10$.

The cases that involve independent screens and strength of turbulence $U = 5$ were run on a Gould Concepts 32/67 computer with an 8500 image-processing board. The ex-

periments took 76 and 57 h, to run for independent screens and $U = 5$, respectively. The study of changing the angle of incidence was conducted on a DEC VAX computer and took 77 h. The last case, for $U = 10$ at 100 realizations, was performed on the San Diego Cray XMP/48 computer and took ~10 min.

6. DISCUSSION

As yet there does not exist a tractable analytical formulation of the backscattered wave problem for a phase screen with a power-law spatial spectrum of index inhomogenieties. Although Jakeman's analysis dealt with the scattering phenomenon due to a Gaussian spatial-correlation function, it can be considered to be an approximation to a power-law spectrum with a finite outer scale, i.e. a lowest spatial frequency.[14] The simulation performed here included an inner and an outer scale only through the maximum grid size and minimum spacing between pixels. The Gaussian power spectrum is defined by a single inhomogeneity scale, so if the illumination of the random phase screen greatly exceeds this
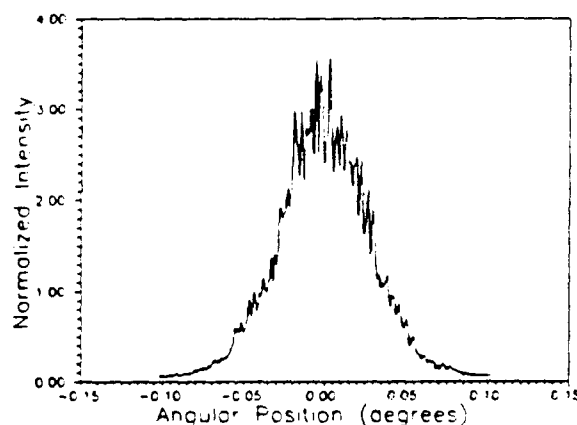

Fig. 3. Angular distribution of the far-field intensity of the backscatter for two independent phase screens, with $U = 10$, $\lambda = 1$ μm, $d = 20$ m, and mirror size = $100\Delta x \times 100\Delta y$ for 80 realizations.
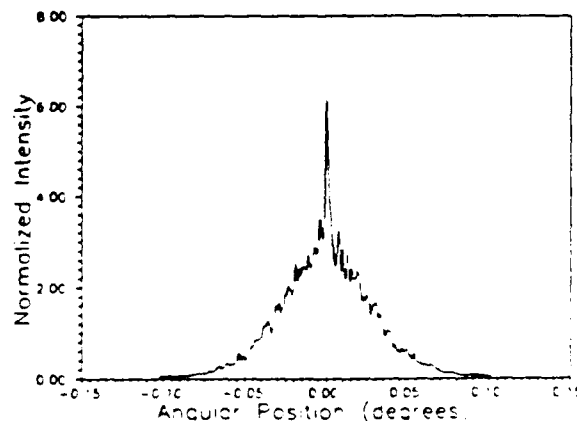

Fig. 4. Angular distribution of the far-field intensity of the backscatter for a normally incident wave with $U = 10$, $\lambda = 1$ μm, $d = 20$ m, and mirror size = $100\Delta x \times 100\Delta y$ for 100 realizations.
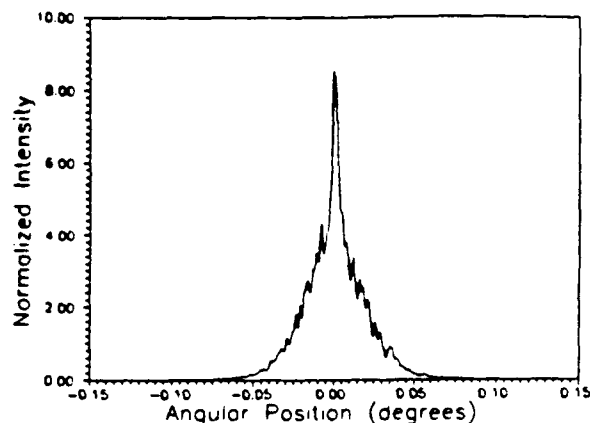
Fig. 5. Angular distribution of the far-field intensity with the same parameters given in Fig. 4 for $U = 5$.
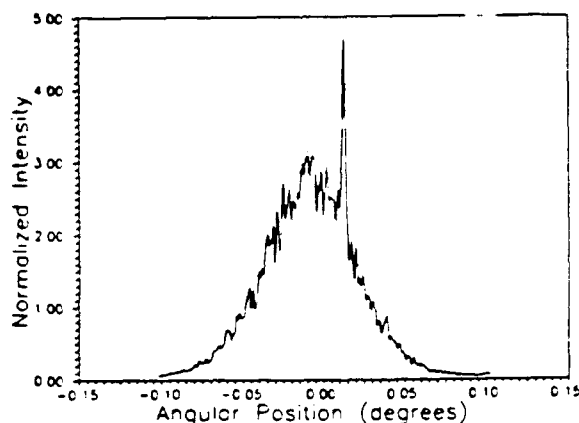

Fig. 6. Angular distribution of the far-field intensity for a wave incident at an angle of 0.012 deg with the same parameters as in Fig. 4 except for 110 realizations.

scale the scattered optical field can truly approach Gaussian speckle. The scattering, which is due to a power-law spatial spectrum, approaches a Gaussian speckle as a limit distribution only at an infinite distance from the screen because of the presence of infinitely large scales of inhomogeneities. The Gaussian power-law spectrum also may manifest strong caustics, whereas a true power-law spectrum does not do so.

The width of the enhancement peak for the weaker screen is approximately twice that of the strong screen. This proportionality of the width to the scattering strength is consistent with the prediction for the Gaussian spectrum screen as given by Eq. (9). The scattering disk is the area of the phase screen that encompasses all the scattering that contributes to a particular point at the mirror. The radius of this disk is given by $\theta_s z$, where θ_s is the width of the angular spectrum and z is the distance to the mirror. The angle $\theta_s = 1/ks_0$, where $k = 2\pi/\lambda$ and s_0 is the width of the mutual coherence function defined by equating the plane-wave structure function to 2, i.e., $D_p(s_0) = 2$. For our case then we have

$$\theta_s = \frac{(3U)^{3/5}}{2\pi}\left(\frac{\lambda}{z}\right)^{1/2}.$$

The angular width of the intensity-enhancement pattern is determined by the diffraction width of the scattering disk. Only rays separated by, at most, the diameter of the scattering disk can have reciprocal paths and add coherently. Hence the scattering disk determines the equivalent aperture for the enhancement and thereby its angular width. The far-field enhancement width is $\theta_e = 2.44 \lambda/D$, where D is the scattering disk diameter, $D = 2\theta_s z$. Theoretically, there is a factor of 1.5 from $U = 10$ to $U = 5$ in the width of the enhancement. Measuring the width at 50% below the peak so as not to have contamination from the normal scattering, we find that the factor between the two strengths is ~ 2.0. This difference may be contributed to the additional diffraction from the finite mirror size of the simulation. Calculations show that the diffraction from the mirror is $\sim 30\%$ of the theoretical enhancement width. Hence, by taking this factor into account, we find that the width agrees with the results from the numerical experiment.

For both the weak- and strong-scattering screens the height of the enhancement peak is approximately twice that of normal scatter. The enhancement predicted by Eq. (9) in the backward direction, $Q = 0$, is twice that of the incoherently scattered angular pattern. There seems to be good agreement between the theory for the Gaussian spectrum screen and the power-law screen of the simulation. Hence the essence of the phenomenon does not seem to be dependent on the details of the phase-screen spectrum.

ACKNOWLEDGMENTS

REFERENCES

1. E. Jakeman, "Enhanced backscattering through a deep random phase screen," J. Opt. Soc. Am. A 5, 1638–1648 (1988).
2. E. Jakeman, P. R. Tapster, and A. R. Weeks, "Enhanced backscattering through a deep random phase screen," J. Phys. D 21, 32–36 (1988).
3. P. R. Tapster, A. R. Weeks, and E. Jakeman, "The observation of backscattering enhancement through atmospheric phase screens," J. Opt. Soc. Am. A 6, 517–522 (1989).
4. V. I. Tatarski, "Some new aspects in the problem of waves and turbulence," Radio Sci. 22, 859–865 (1987).
5. I. B. Esipov and V. V. Zosimov, "Observation of partial phase conjugation in the case of reflection in a randomly inhomogeneous medium," Opt. Spectrosc. (USSR) 60, 234–236 (1986).
6. Y. A. Kravtsov and A. I. Saichev, "Effects of double passage of waves in randomly inhomogeneous media," Sov. Phys. Usp. 25, 494–508 (1982).
7. J. P. Filice, "Studies of the microscale density fluctuations in the solar wind using interplanetary scintillations," Ph.D. dissertation. (University of California, San Diego, San Diego, Calif., 1984).

8. C. L. Rino, "Numerical computations for a one dimensional power law phase screen," Radio Sci. 15, 41–47 (1980).

9. J. M. Martin and S. M. Flatté, "Intensity images and statistics from numerical simulation of wave propagation in 3-D random media," Appl. Opt. 27, 2111–2126 (1988).

10. H. G. Booker, J. A. Ferguson, and H. O. Vats, "Comparison between the extended medium and the phase screen scintillation theories," J. Opt. Soc. Am. A 47, 381–399 (1985).

11. R. L. Phillips, L. C. Andrews, E. Jakeman, and J. G. Walker, "The statistical properties of laser light scattered by two phase

screens," in Acquisition, Tracking and Pointing, R. R. Avelmann and H. L. Richard, eds., Proc. Soc. Photo-Opt. Instrum. Eng. 642, 282–285 (1986).

12. A. Ishimaru, Wave Propagation and Scattering in Random Media (Academic, New York, 1978), Vol. 2, p. 409.

13. V. H. Rumsey, "Scintillations due to a concentrated layer with a power-law turbulence spectrum," Radio Sci. 10, 107–114 (1975).

14. H. Booker and G. Majicliahi, "Theory of refractive scattering in scintillation phenomena," J. Atmos. Terr. Phys. 43, 1199–1204 (1981).

5. IR FOCAL PLANE ARRAY TESTING

Glenn Boreman, Ph.D
Infrared Systems Laboratory/CREOL

5.1 Background

CREOL's Focal Plane Array testing program consists of the measurement of various specific detectors, the development of various instrumentation devices for the measurement of detector modulation transfer functions (MTFs), the development of an IR scene projector system, as well as the development of data processing and computing facilities.

The types of detectors that have been tested include an ISTEF provided Mitsubishi Platinum Silicide CCD camera, a CREOL Mitsubishi PtSi CCD, a Signal Processing In The Element (SPRITE) Detector, a silicon CCD staring array, and hexagonal array structures.

Unique instrumentation has been developed for the measurement of the MTF of three detector architectures: 1) self-scanned arrays, 2) SPRITE detectors, and 3) staring arrays.

An IR scene projector instrument has been developed to provide complex realistic images to the system array under test. The goal of this system is to provide a realistic time history, dynamic range, and resolution in response to an externally generated video source.

The computing facilities have been upgraded from an IBM PC AT to a SUN 330 workstation with future plans to implement a fiber link to the University's SUN network.

5.2 Characterization of Mitsubishi Platinum Silicide CCD Camera

An important component of the infrared imaging system at ISTEF is the 512x512 PtSi charge-coupled device (CCD) array from Mitsubishi. This camera was borrowed from ISTEF on two occasions. Extensive test data were collected during that limited period. The data from those measurements yielded calibration information for the camera. Specific tests performed measured uniformity, linearity, responsivity, and mean-variance.

The experimental setup for each characterization used a 2.5-mm-diameter 1000 K blackbody

36

source. The distance from the blackbody source to the CCD array was varied to produce a complete range of irradiances on the array. The small source size produced uniform illumination over the detector array (flat-field inputs). No lens was used in this setup; thus the flux from the blackbody followed a well-defined inverse-square dependence. The passband of the system was 3 to 5 μm, defined by the Dewar window.

5.2.1 Uniformity

Figure 5-1 is an example of the raw array output, with a flat-field input. The spatial noise pattern is typical of uncorrected output from PtSi CCDs[1] and represents a 3% nonuniformity (standard deviation divided by maximum dynamic range). When the internal camera calibration is enabled (correction for gain and offset), the output produced for a flat-field input is uniform to well below 1%.

5.2.2 Linearity

Figure 5-2 illustrates response in pixel count plotted against focal-plane irradiance in W/cm^2. The camera response is linear at high irradiance levels, until the saturation limit of the camera is reached. Minor departures from linearity occur at low irradiance levels, and can be corrected by using look-up tables.

5.2.3 Responsivity

The slope of the curve in the linear regime yields a responsivity of 1.5×10^{-7} W cm^{-2} pixel count^{-1}, which agrees with the Mitsubishi specification for responsivity.

5.2.4 Mean Variance

For each frame of data representing a particular blackbody distance, the variance of the pixel count is plotted against the mean. Figure 5-3 shows the resulting mean-variance curve,[2] which indicates whether or not the array is operating under background-limited (BLIP) conditions. If the primary contribution to the variance is the photon noise on the background, then the plot of mean versus variance will be linear, consistent with Poisson statistics. Our data in Figure 5-2 indicate that the Mitsubishi CCD imager is not BLIP for focal-plane irradiances below approximately 20×10^{-6} W/cm^2.

To properly support this program, we purchased a Mitsubishi PtSi array identical to that
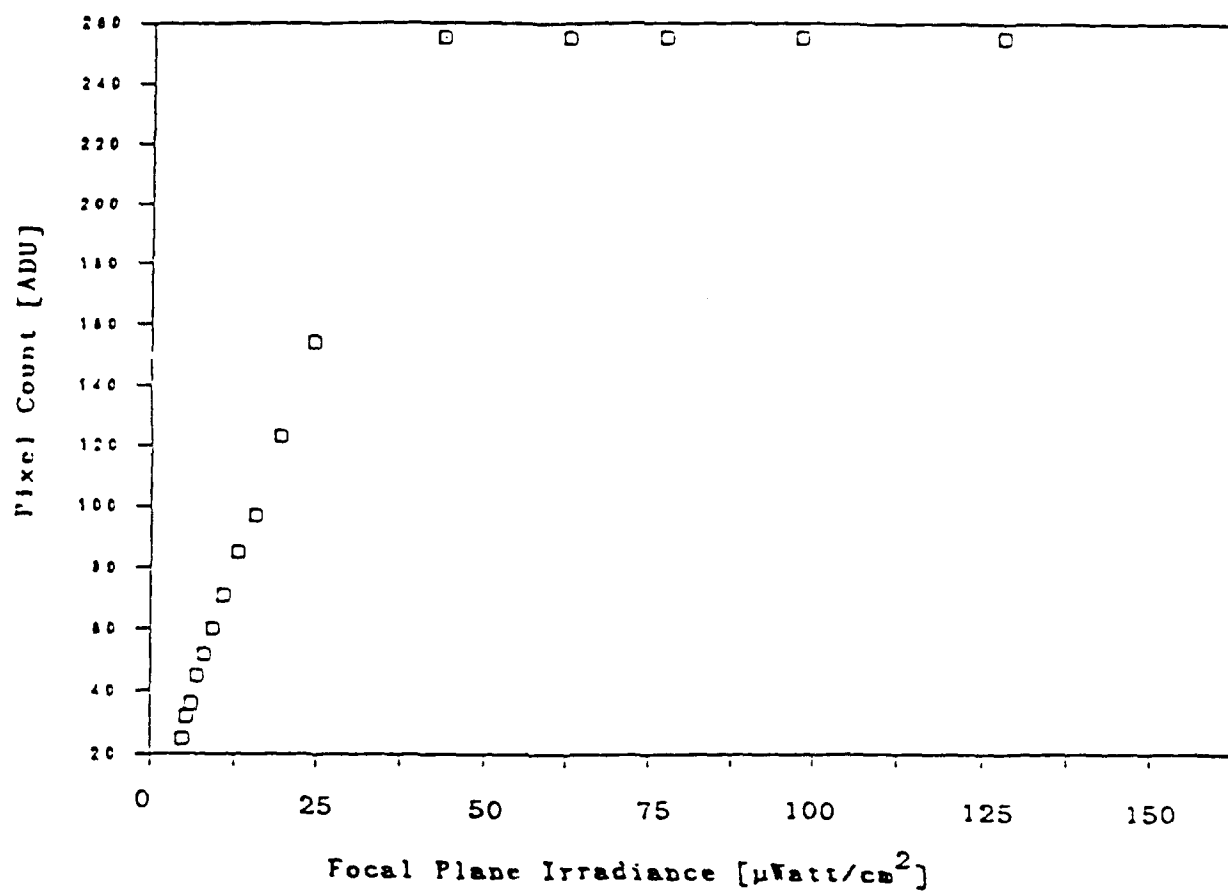
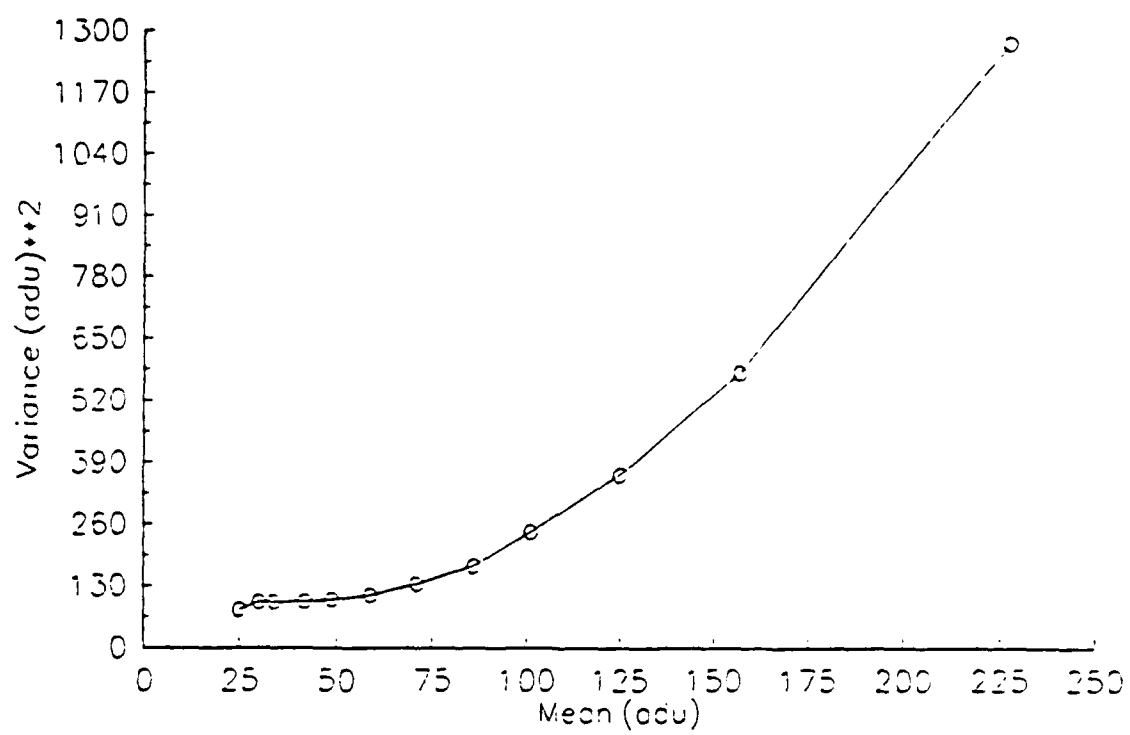Figure 5-2. Linearity plot for PtSi CCD array.

Figure 5-3. Mean-Variance Curve for PtSi CCD

40

residing at ISTEF. Thus we can continue the characterization of performance without interruption of ISTEF data-acquisition activities. The acquisition of this equipment was supported by CREOL research initiation funds.

5.3 Focal Plane MTF Research

The modulation transfer function (MTF) is perhaps the most useful figure of merit for electro-optical systems. A specification of image quality in the spatial-frequency domain provides a flexibility and an ease of analysis unmatched by a spatial-domain description. MTF allows the convenient cascading of various subsystems by a simple multiplication of their transfer functions, rather than by the convolution of an equivalent number of impulse responses.

Focal plane arrays remain one important subsystem for which the application of MTF techniques is still under development. While classical optical systems are well described by conventional MTF theories, focal plane arrays have a number of complicating factors related to aliasing, finite sampling windows, charge transfer inefficiency, crosstalk, and system noise. In addition, even the instrumentation necessary for the measurement of MTF for focal plane arrays is still a subject of research.

The research on MTF of focal plane arrays at CREOL separates into three areas, each of which will be discussed separately. These include: development of MTF instrumentation for self-scanned arrays; development of MTF instrumentation for staring arrays; and analysis of the hexagonal-array MTF.

5.3.1 MTF Instrumentation Development - Self-Scanned Arrays

SPRITE detectors are self-scanned detector structures that are usually found in linear focal plane arrays. SPRITE technology is currently being used in a number of infrared imaging systems in the 8-10 μm waveband as an interim solution until staring focal-plane technology matures for HgCdTe. SPRITE technology represents a viable alternative for ISTEF's long-wave infrared imaging needs.

A SPRITE detector, seen in Fig. 5-4, consists of a strip of photoconductive material operated under a constant current bias. Photogenerated carriers will drift along the structure at a rate determined by the applied voltage and the carrier mobility. If the IR image is scanned across the detector structure at the same rate as the carrier drift velocity, the signal-to-noise ratio is increased because of signal averaging.
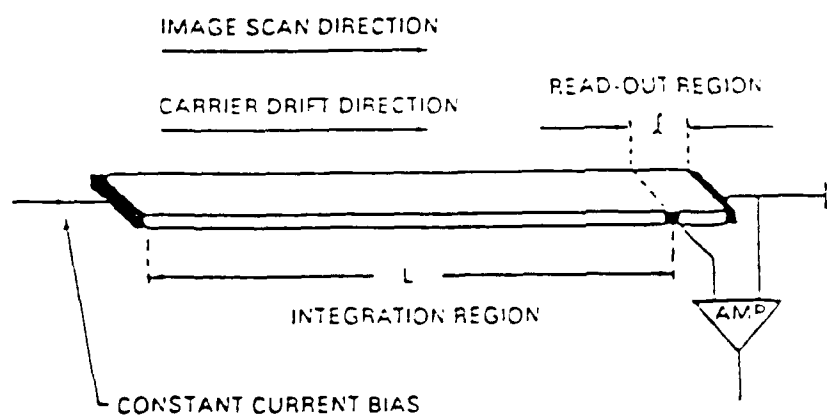
IMAGE SCAN DIRECTION

CARRIER DRIFT DIRECTION

READ-OUT REGION

L

INTEGRATION REGION

CONSTANT CURRENT BIAS

AMP

Figure 5-4. SPRITE detector configuration

42

During the past year, we developed instrumentation (Fig. 5-5) to measure the MTF of SPRITEs by means of the sine-wave response. An infrared He-Ne laser (wavelength 3.39 μm) is used in conjunction with a set of double-slit apertures to project interference fringes of variable spatial frequency onto the SPRITE. The fringes are scanned at an appropriate velocity with a polygon scanner. The MTF is measured from the modulation depth of the resulting signals as a function of frequency.

Our results on the MTF of SPRITE detectors (Fig. 5-6) have confirmed an expected theoretical dependence[3] of MTF on the length of the detector (longer detector yields poorer MTF because of charge diffusion). We have submitted an article[4] on this measurement method, which is included as Appendix A.

This type of target generator will also be useful to the ISTEF mission in unconventional imaging. The developmental system to evaluate the performance of the unconventional imaging systems will require a means to generate interference fringes of variable spatial frequency and contrast level.

5.3.2 MTF Instrumentation Development - Staring Arrays

Staring focal plane arrays are a key technology element for the infrared imaging systems of the future. The advantages in compactness, size and weight, mechanical simplicity, and sensitivity indicate that this class of image receiver will be the new standard, surpassing the scanned FLIR systems so prevalent today. Indeed, for many ISTEF missions in target location, imaging spectroscopy, and unconventional imaging, staring arrays are the central component to determining the ultimate performance of these systems.

We have developed a new technique to measure the MTF of staring focal plane arrays, both in the visible and infrared portions of the spectrum. The basic technique[5] consists of projecting a laser speckle of known spatial frequency content onto the focal plane array. The spatial power spectral densities (PSDs) of the speckle patterns, before and after detection, are related by the MTF of the CCD array:

$$PSD_{out}(\xi) - PSD_{in}(\xi) \; |MTF(\xi)|^2 \tag{5-1}$$

where ξ is the spatial frequency. We have developed[4] an extension of the basic method for speckle generation that employs an integrating sphere as the phase-randomizing medium, rather than a ground-glass diffuser. Figure 5-7 is a schematic of the measurement setup. The integrating-sphere
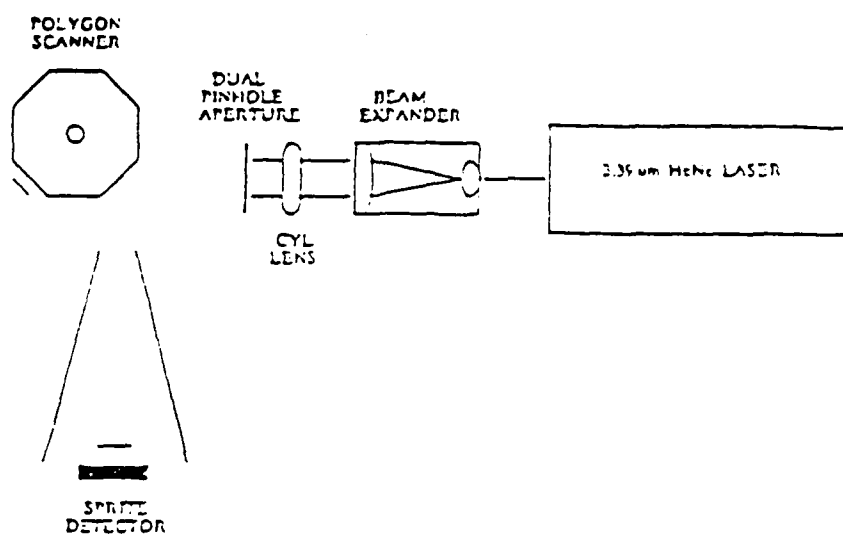
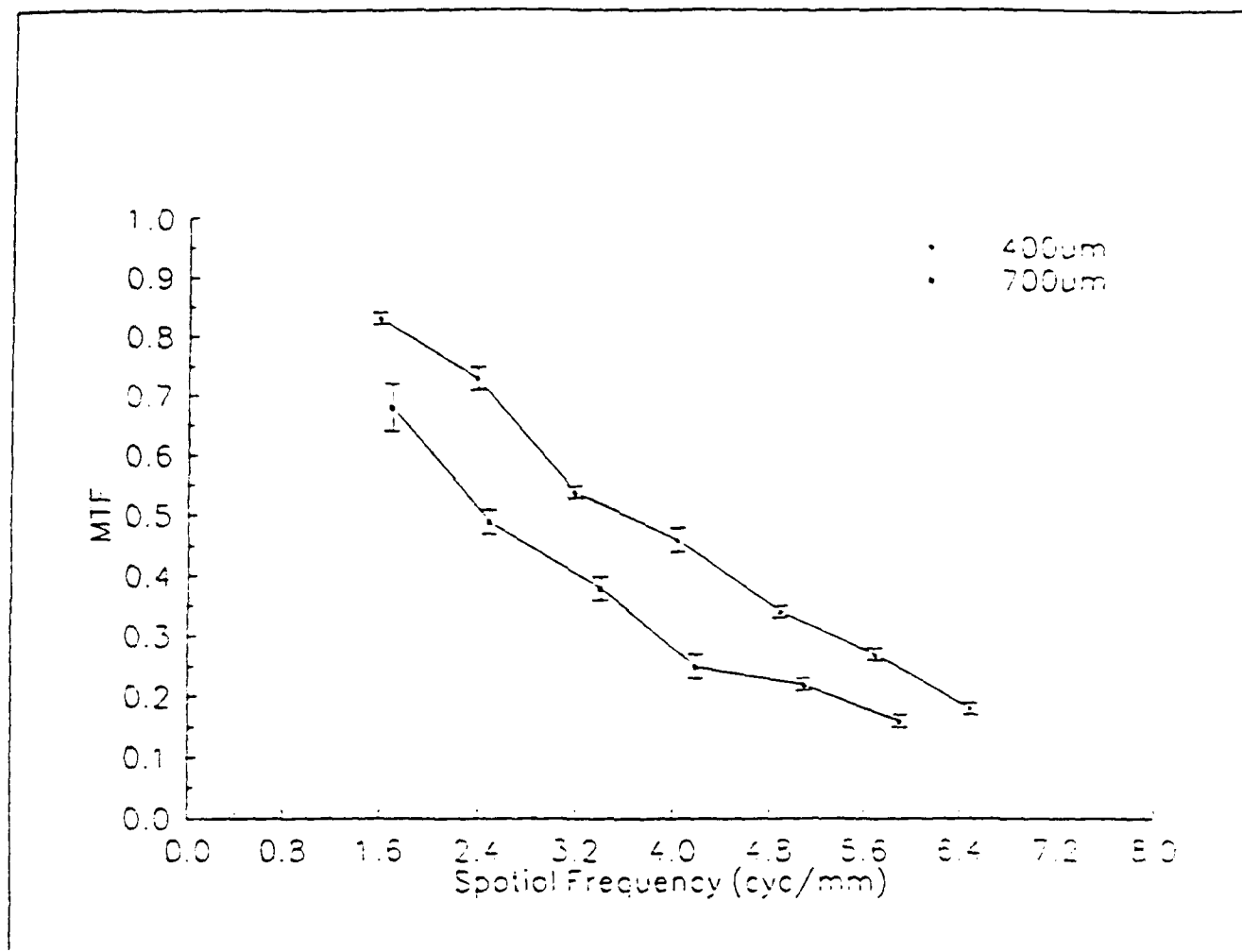Figure 5-5. MTF instrumentation developed for SPRITEs

44

Figure 5-6. Results of MTF measurement for SPRITEs.
Note the decrease in MTF for longer SPRITE element length

approach is particularly useful at infrared wavelengths.

Our current research in this area involves the development of techniques that allow the MTF to be measured past the spatial Nyquist frequency of the focal plane array. This requires a capability to generate a speckle pattern with a flat bandpass characteristic to avoid artifacts in the data that would result from aliasing. Briefly, the PSD of the speckle is proportional to the autocorrelation of the aperture that generates the speckle.[7] We use a nonseparable aperture (Fig. 5-8) that has a substantial flat region of autocorrelation (Fig. 5-9) to produce the flat bandpass. In Fig. 5-10 we show the full two-dimensional PSD_{out}, which has been modified by the CCD MTF. We are currently developing the technique using a silicon CCD at a wavelength of 0.8 μm, and have purchased components to extend these tests to the platinum silicide camera at 3.39 μm. An article is being prepared on this research for submission to *Optical Engineering*.

In addition to the importance of laser speckle to the MTF research, the availability of a calibrated speckle generator will prove useful to the ISTEF mission in unconventional imaging. Our techniques facilitate the production of speckle patterns over a wide range of wavelengths that have well-known statistics and well-defined spatial-frequency contents. One component of the developmental system to evaluate the performance of ISTEF's unconventional imaging systems will be a speckle generator using the integrating sphere configuration.

5.3.3 Analysis - Hexagonal Staring Arrays

We analyzed and compared MTFs obtained from a hexagonal array of hexagonal detectors and a hexagonal array of rectangular detectors (Fig. 5-11). Hexagonal detector arrays are valuable in super-centroiding applications,[8,9] facilitating more efficient and robust super-centroiding algorithms because of the symmetric nature of the lattice.

We considered the spatial averaging that occurs over the surface of the photosite, and cast it as a convolution of the spatial photosite responsivity and the incident irradiance distribution. Then, operating in the Fourier domain, the MTF attributable to this spatial averaging is seen.

Our results are shown in Fig. 5-12. The MTF in the vertical direction is enhanced ($\approx$ 10% MTF increase at Nyquist), at the expense of the horizontal MTF ($\approx$ 5% MTF decrease at Nyquist).

The MTF of these structures has not been previously presented in the literature, and we have submitted an article[10] to *Applied Optics* as a result of this research (see Appendix B).
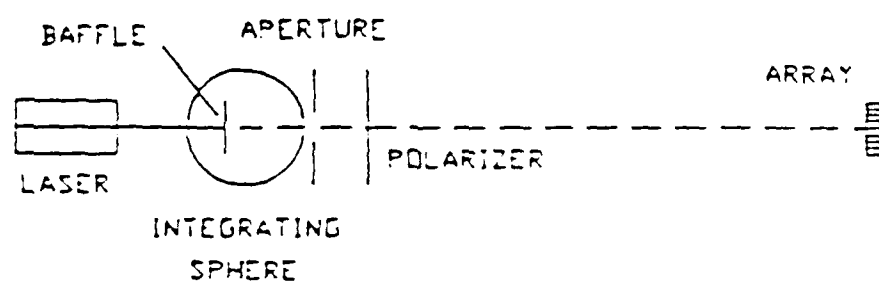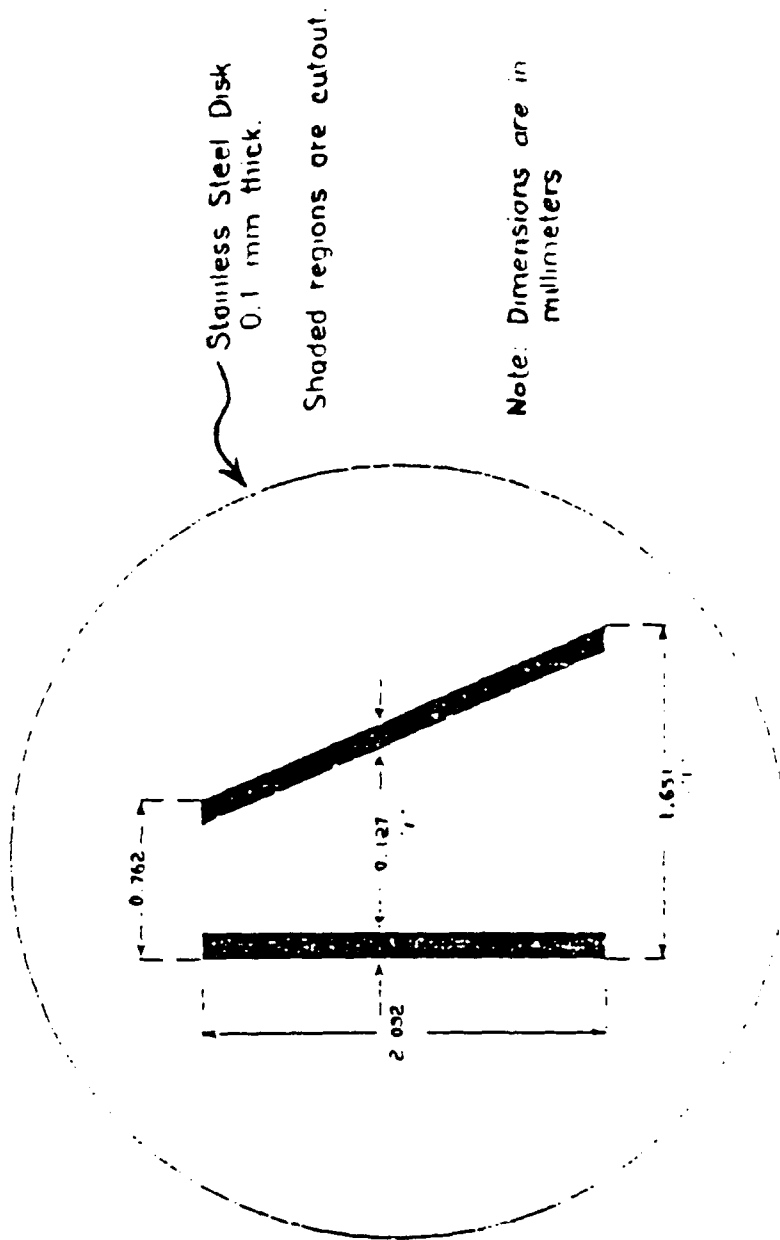
Figure 5-7. Schematic of MTF measurement setup.

Aperture for Speckle Generator

Stainless Steel Disk
0.1 mm thick.

Shaded regions are cutout.

Note: Dimensions are in millimeters

0.762

0.127

1.651

2.032

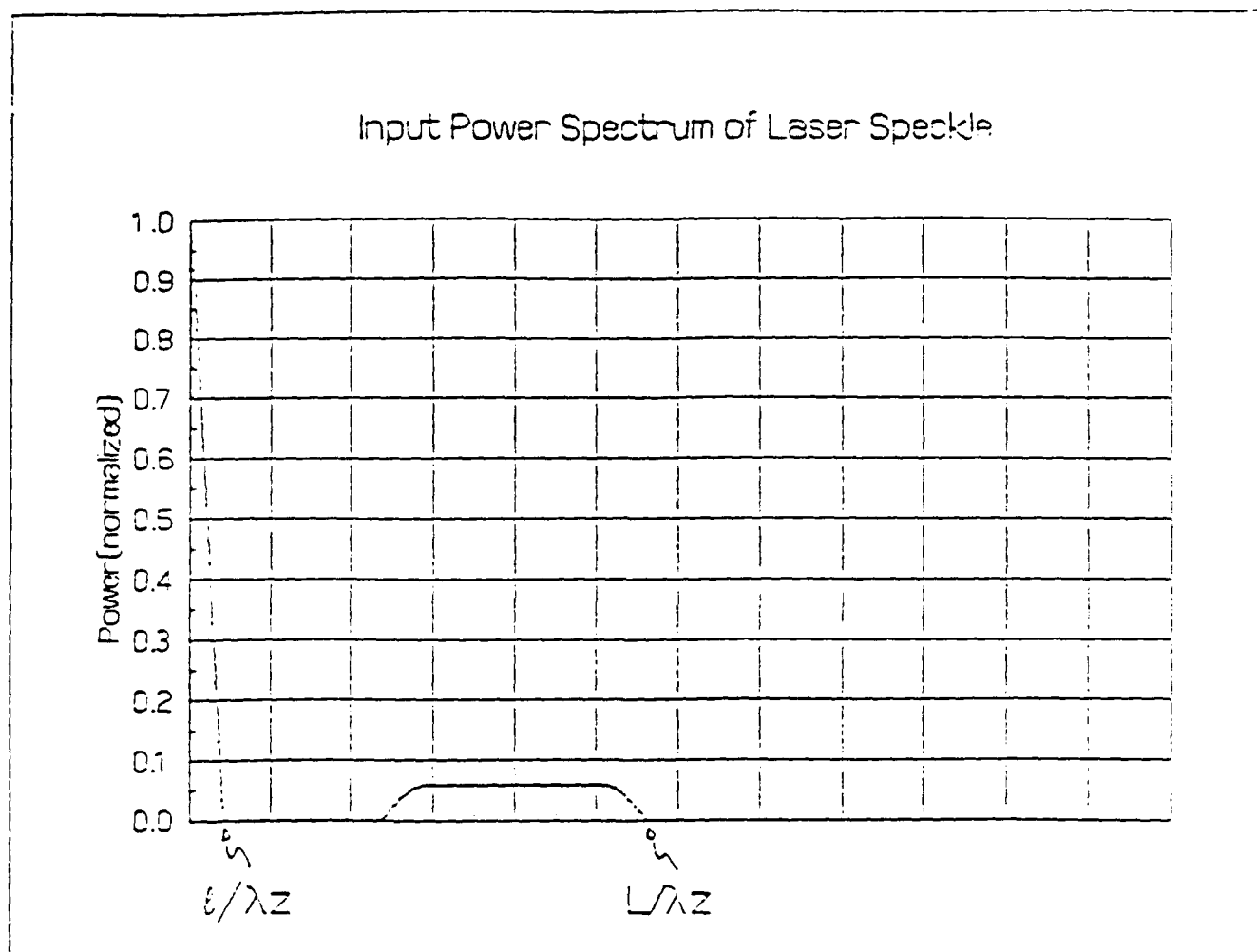Figure 5-8. Nonseparable aperture for the speckle generator

48

Figure 5-9. Input power spectral density for the laser speckle which results from the use of the aperture in Fig. 5-8. Note the flat bandpass region. L is the largest separation in the aperture, l is the width of the slits, Z is the distance from the aperture to the focal plane, and λ is the wavelength.

Figure 5-10. Two dimensional power spectral density of the laser speckle, after processing by the CCD array. The portions of the spectrum removed from the central cross structure are the flat bandpass portions of the speckle seen in 1D in Fig. 5-9. The shading seen in these sections is caused by the MTF of the array.
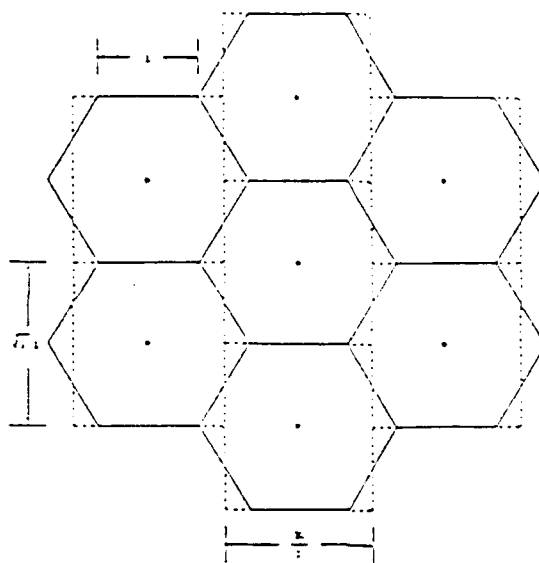
50

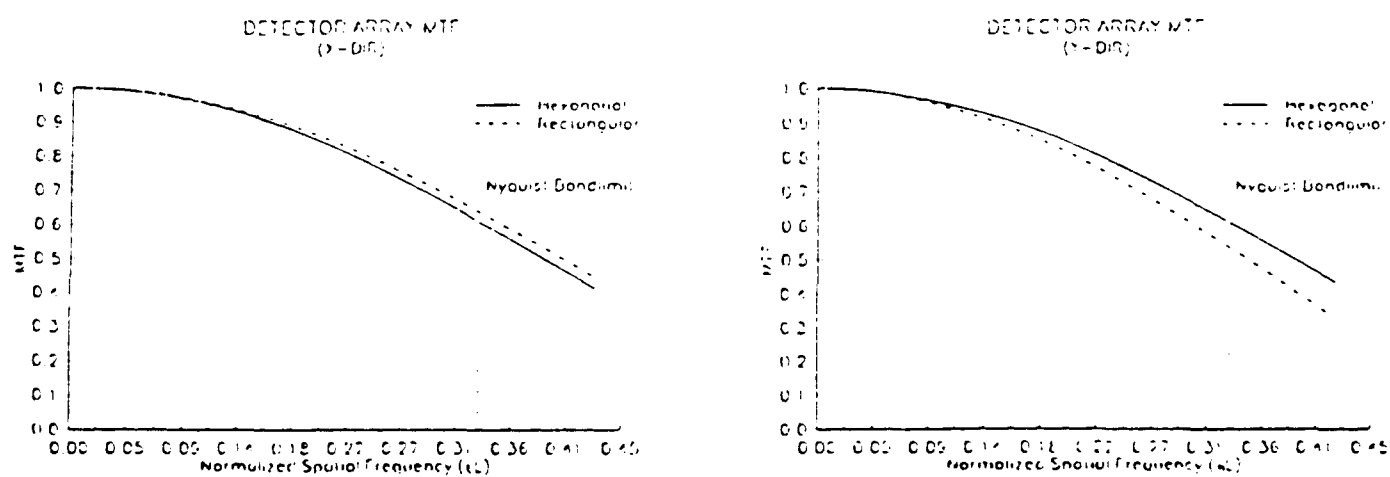Figure 5-11. Geometry of the hexagonal arrays investigated.

Figure 5-12. MTF results for the hexagonal detectors and rectangular detectors seen in Fig. 5-11. The hexagonal detectors have a larger MTF in the vertical direction than do the rectangular detectors. The rectangular detectors have a smaller MTF advantage in the horizontal direction.

52

5.4 Target Projector Development

A central issue facing the users of infrared systems is end-to-end performance characterization, including the optics, focal plane array, electronics, and data-processing algorithms. The desired test images are becoming more complex. The usual bar charts, impulse response tests and broad-area thermal sensitivity measurements must be coupled with the presentation of realistic infrared scenes to the system under test. Infrared scene projection is an effective tool for system-performance characterization, without the need for expensive and time-consuming field trials.

The central technical problem is to create infrared scenes of realistic time history, dynamic range, and resolution in response to an externally generated video source. We are vigorously pursuing research that shows promise of filling this need.

The projector system seen in Fig. 5-13 (on long-term loan to CREOL from the Naval Training Systems Center) is a raster-scanned CO_2 laser operating at 10.6 μm. The laser is acousto-optically modulated in response to video rate input, and a two-dimensional beam scan is performed to directly write the infrared scene into the entrance aperture of a thermal imager system. The projector MTF is a function of both the modulator drive format[11] and the laser beam profile.[12]

Currently we are performing MTF measurements on this system that investigate the additional effect of acoustic wave decay in the modulator cell. We have presented a paper on this topic at the March 1991 SPIE meeting on Aerospace Systems in Orlando.

In addition to the utility of this research for imager characterization, this target-projection technology will also be used in the test-bed system for evaluating the performance of unconventional imaging systems for ISTEF.

5.5 Computer System Development

The characterization of focal plane arrays requires digital processing of high-resolution data sets. Until last year, we had performed this processing on IBM AT-class machines. The volume of data dictated that we progress to a more capable data-processing computer. With joint funding from ONR and the Florida High Technology Council, we obtained a SUN 330 workstation. The typical processing time for the 512x512 data sets has decreased by more than an order of magnitude. We are currently pursuing additional storage media, and access to the UCF campus network by means of a fiber-optic link from the Research Park. Also, we have ordered a comprehensive
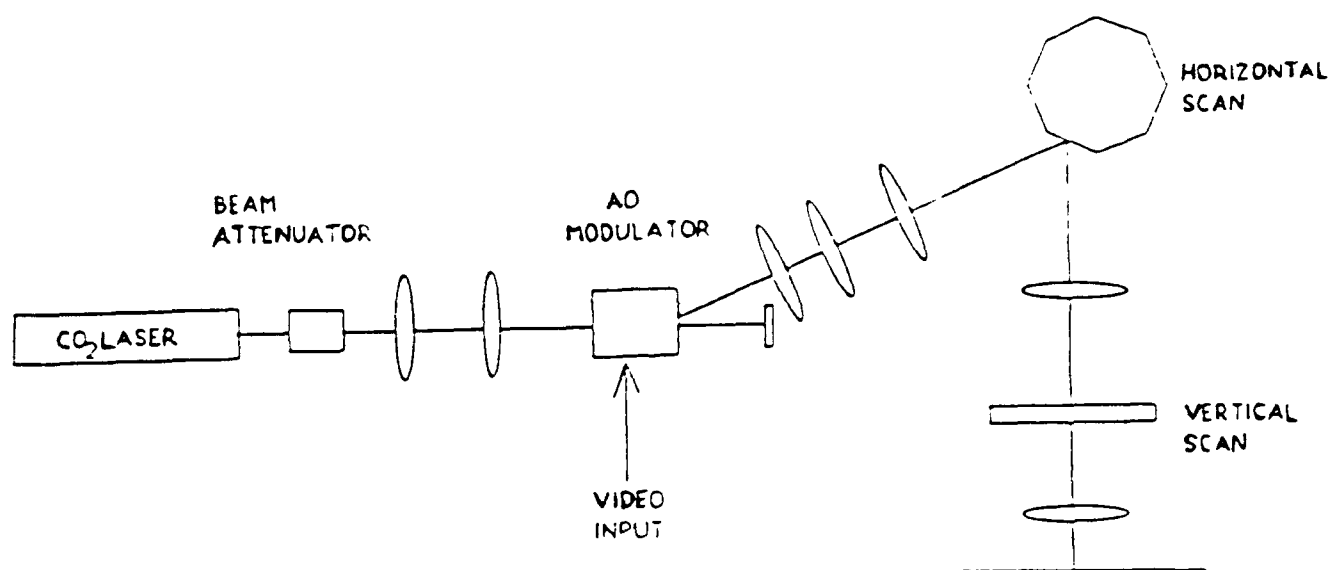
Figure 5-13. CO_2 Laser-Based Scene Projector

54

data-processing/math software package using CREOL research initiation funds. This system promises to fill the needs of the focal-plane-array research program in terms of data acquisition, processing, display, storage, and experimental control for the foreseeable future.

The SUN format has been used at the main ISTEF sites and by other ISTEF research groups at UCF. Adoption of this format will increase the sharing of data and software among the participating groups.

5.6 References

1. J. Murguia, J. Mooney, and W. Ewing, "Evaluation of a PtSi infrared camera," *Opt. Eng.* 29, 786 (1990).

2. L. Mortara and A. Fowler, "Evaluations of CCD performance for astronomical use," *Solid State Imagers for Astronomy, Proc.* SPIE 290, 28 (1981).

3. G. Boreman and A. Plogstedt, "MTF and number of equivalent elements for SPRITE detectors," *Appl. Opt.* 27, 4331 (1988).

4. K. Barnard and G. Boreman, "MTF measurement of SPRITE detectors: sine wave response," submitted to *Appl. Opt.*

5. G. Boreman and E. Dereniak, "Method for measuring MTF of CCDs using laser speckle," *Opt. Eng.* 25, 148 (1986).

6. G. Boreman, Y. Sun, and A. James, "Generation of laser speckle with an integrating sphere," *Opt. Eng.* 29, 339 (1990).

7. J. Goodman, in *Laser Speckle and Related Phenomena*, J. C. Dainty, ed., pp. 46-58 (Springer-Verlag, Berlin, 1975).

8. J. Cox, "Point source location using hexagonal detector arrays," *Proc. SPIE* 686, 130 (1986).

9. J. Cox, "Advantages of hexagonal detectors and variable focus for point source location," *Proc. SPIE* 750, 62 (1987).

10. K. Barnard and G. Boreman, "Two-dimensional MTF of hexagonally sampled detector arrays," submitted to *Appl. Opt.*

11. R. V. Johnson, "Scophony light valve," *Appl. Opt.* 18, 4030 (1979).

12. J. Randolph and J. Morrison, "Modulation transfer characteristics of an A/O deflector," *Appl. Opt.* 10, 1383 (1971).